INTERFACE

rsif.royalsocietypublishing.org

Research

Cite this article: Zhao J, Cao Y, DiPietro LA, Liang J. 2017 Dynamic cellular finite-element method for modelling large-scale cell migration and proliferation under the control of mechanical and biochemical cues: a study of re-epithelialization. *J. R. Soc. Interface* **14**: 20160959.
http://dx.doi.org/10.1098/rsif.2016.0959

Received: 29 November 2016
Accepted: 15 March 2017

Subject Category:
Life Sciences–Mathematics interface

Subject Areas:
biophysics, biomathematics, computational biology

Keywords:
collective cell migration, re-epithelialization, dynamic cellular finite-element model, cell migration and proliferation, cellular mechanics, tissue modelling

Author for correspondence:
Jie Liang
e-mail: jliang@uic.edu

Electronic supplementary material is available online at https://dx.doi.org/10.6084/m9.figshare.c.3726151.

THE ROYAL SOCIETY PUBLISHING

Dynamic cellular finite-element method for modelling large-scale cell migration and proliferation under the control of mechanical and biochemical cues: a study of re-epithelialization

Jieling Zhao[1], Youfang Cao[3], Luisa A. DiPietro[2] and Jie Liang[1]

[1]Department of Bioengineering, and [2]Center for Wound Healing and Tissue Regeneration, College of Dentistry, University of Illinois at Chicago, Chicago, IL, USA
[3]Theoretical Biology and Biophysics (T-6), Center for Nonlinear Studies (CNLS), Los Alamos National Laboratory, Los Alamos, NM, USA

JZ, 0000-0002-9801-2434; YC, 0000-0002-5880-0006; JL, 0000-0002-2773-6427

Computational modelling of cells can reveal insight into the mechanisms of the important processes of tissue development. However, current cell models have limitations and are challenged to model detailed changes in cellular shapes and physical mechanics when thousands of migrating and interacting cells need to be modelled. Here we describe a novel dynamic cellular finite-element model (DyCelFEM), which accounts for changes in cellular shapes and mechanics. It also models the full range of cell motion, from movements of individual cells to collective cell migrations. The transmission of mechanical forces regulated by intercellular adhesions and their ruptures are also accounted for. Intra-cellular protein signalling networks controlling cell behaviours are embedded in individual cells. We employ DyCelFEM to examine specific effects of biochemical and mechanical cues in regulating cell migration and proliferation, and in controlling tissue patterning using a simplified re-epithelialization model of wound tissue. Our results suggest that biochemical cues are better at guiding cell migration with improved directionality and persistence, while mechanical cues are better at coordinating collective cell migration. Overall, DyCelFEM can be used to study developmental processes when a large population of migrating cells under mechanical and biochemical controls experience complex changes in cell shapes and mechanics.

1. Introduction

Cells are the basic functional elements of living bodies. Cell–cell and cell–environment interactions largely maintain biological tissues [1]. Many experiments have been performed to understand the mechanisms behind cellular interactions, cell behaviours and tissue patterning [2]. However, many subcellular processes such as cytoskeleton generated physical forces and cell–cell transmitted mechanical forces are difficult to access experimentally [3]. Computational modelling of cell–cell and cell–environment interactions, therefore, provide useful means of investigations that complement experimental studies to answer questions such as how cellular border forces between cell and environment control the closure of epithelial gaps [3], and how cell shape influences the field of traction force [4].

A number of computational cell models have been developed [5–18]. These models can be broadly categorized into continuum and discrete models. Continuum models are based on differential equations to model the spatial–temporal changes of protein density in cells, and changes of cell populations in a tissue. In these models, individual cells and interactions are not considered

explicitly [5–7]. Discrete models such as the cellular Potts model [8–10], vertex model [11,12,19–21], centric model [13], subcellular element model [14], immersed boundary model [15] and finite-element model [16,17] are based on discretized elementary units to model cell morphology and motility. These models can describe cell shape and intercellular interactions explicitly. However, there are many limitations. The cellular Potts model represents each cell as a set of lattice sites [22]. The underlying physical forces and cellular mechanics are difficult to recover from spatial changes of lattice sites. The vertex model describes the changes in cell shape based on minimizing energy under forces acting on cell boundary junctions [11]. The specific cell shape contributing to the mechanical energy of cell interior is usually not considered [11]. The centric model can only describe the shape of a cell as one or two simple spheres [13]. The subcellular element model can describe cell shape in high resolution. However, the distances between intra/intercellular elements are artificially maintained through an arbitrarily imposed Morse potential [14], which is not physically realistic [23]. The immersed boundary model can also describe cell shapes in detail. However, the physical boundary of the cell body may not fully conform to the grid underneath [24], which lead to irregular boundary points in the solution. The finite-element cell model can describe both cell shape and cell mechanics accurately [16,25]. However, this method permits only limited changes in cell shape and allows limited flexibility of cell movement, and therefore is restricted to cellular and tissue processes that do not involve free movement of individual cells. Owing to these limitations, accurate modelling of physiological processes involving large scale and collective cell migration at a detailed cellular level remains a challenging task.

Here we describe a novel dynamic cellular finite-element model (DyCelFEM), which has a number of advantages over existing discrete cell models. It can accurately describe the full span of cell movement, from the free movement of individual cells to large scale collective cell migration. In addition, changes in shapes of moving cells under the control of cell mechanics are fully accounted for. Furthermore, the transmission of mechanical force regulated by intercellular adhesion and its rupture are also explicitly modelled. As biochemical signals strongly influence cell behaviour and tissue patterning [26], intracellular networks of protein signalling are also embedded inside individual cells in our model. Our DyCelFEM model is therefore suited to study biological processes involving large-scale collective cell motion under the regulation of biochemical signals and mechanical forces, with accurate description of cell shapes and cell mechanics.

In this study, we apply DyCelFEM to investigate the effects of biochemical and mechanical cues on migration and proliferation of a population of keratinocyte cells and on tissue patterning using a simplified re-epithelialization model of wound tissue. We examine the directionality and persistence of cell migration, and cell–cell coordination during re-epithelialization under different guidance control mechanisms of cell migration. Our results suggest that the influence of biochemical cues are restricted to areas close to the wound bed, while mechanical cues influence the tissue globally. Furthermore, biochemical cues are better at guiding cell migration with improved directionality and persistence, while mechanical cues are better at coordinating collective cell migration. These findings provide useful information towards understanding the full mechanism of wound healing.

2. Model and methods

2.1. Geometry, discretization, deformation energy and dynamic changes of cells

2.1.1. Geometry and discretization of the cell

In our model, a two-dimensional cell Ω is defined by its boundary $\partial\Omega$, which is represented by an oriented polygon connecting a set of boundary vertices $V_{\partial\Omega} \equiv \{v_i \in \partial\Omega \subset \mathbb{R}^2\}$. The cell boundary $\partial\Omega$ is a closed chain of oriented edges $(e_{1,2}, e_{2,3}, \ldots, e_{n,1})$, where edge $e_{i,i+1}$ connects modulus n consecutive boundary vertices v_i and v_{i+1} in the anticlockwise orientation. We denote the location of a vertex v_i as x_i. We first compute the Delaunay triangulation D_Ω of the cell Ω using only boundary vertices $V_{\partial\Omega}$. We then test if the radius of the circumsphere of any triangle in D_Ω is larger than a threshold. If so, a new vertex is inserted at the circumcenter of this triangle and D_Ω is updated accordingly [27]. This is repeated until all new triangles have their circumsphere radius smaller than a threshold. The cell Ω is therefore represented by a simplicial complex K_Ω, composed of a set of boundary vertices and inserted interior vertices $V_\Omega = V_{\partial\Omega} \cup V_{\mathrm{Int}}$, a set of edges $E_\Omega = \{e_{i,j} \mid v_i, v_j \in V_\Omega\}$ and a set of triangles $T_\Omega = \{\tau_{i,j,k} \mid v_i, v_j, v_k \in V_\Omega\}$ (figure 1*a*,*b*; see more details on in the electronic supplementary material, text S1).

2.1.2. Deformation energy of the cell

We use $u(x)$ to represent the deformation vector of the cell at x, strain tensor $\epsilon(x)$ to describe the local deformation at x and the stress tensor σ to represent the forces at x. During cell motility, we assume that the recovery of cell shape is incomplete due to the plastic deformation originating from bond ruptures within the cytoskeleton as shown in [28]. For simplicity, we assume cell is linearly elastic during each time step and is plastic between time steps. Therefore, we re-calculate the triangular mesh T_Ω for each cell Ω after each time step and reset the stress to zero after location update (see discussion on the reason that viscoelasticity can be neglected in electronic supplementary material, text S1).

The overall free energy E_Ω of cell Ω is given by the sum of elastic energy E_{el}, contractile energy E_{co}, adhesion energy E_{ad} and force energy E_{f}.

The elastic energy takes the form $E_{\mathrm{el}} = \frac{1}{2}\int_\Omega \sigma^{\mathrm{T}}(x)\epsilon(x)\,\mathrm{d}x$. The contractile energy arising from the contractility of the cell takes the form $E_{\mathrm{co}} = -\int_\Omega(\sigma_a, \sigma_a, 0)\epsilon(x)\,\mathrm{d}x$, where σ_a is a homogeneous contractile pressure resulting from active bulk process [4]. Using Gauss' divergence theorem, it can be further written as $-\int_\Omega(\sigma_a, \sigma_a, 0)\epsilon(x)\,\mathrm{d}x = -\int_{\partial\Omega}\sigma_a n(x)^{\mathrm{T}}u(x)\,\mathrm{d}x$.

The adhesion between the cell and substratum contributes to the total energy of the cell. We follow [4] and assume that the adhesion force F_{a} generated from the substratum on the cell is proportional to the displacement u according to Hooke's Law of $F_{\mathrm{a}} = Yu$. The L_2 norm of the displacement field gives the adhesion energy E_{a} as $E_{\mathrm{a}} = \frac{1}{2}Yu^2$, where Y is a constant parameter proportional to the stiffness of substratum and to the strength of focal adhesion between cell and the substratum [4].

The boundary adhesion energy between neighbouring cells is proportional to the size of the contacting surfaces following [29]. Specifically, the adhesion energy between a cell Ω and the set of its neighbouring cells $\{\Omega_i\}$ takes the form of $\sum_{i,\Omega\bigcap\Omega_i\neq\varnothing}\int_{\Omega\bigcap\Omega_i} f_a n(x)^{\mathrm{T}}u(x)\,\mathrm{d}x$, where $n(x)$ is the surface normal vector at x, and f_{a} is a constant adhesion force per unit length along the cell–cell boundary. This constant adhesion force occurs when the adhesive contact is formed on the cell–cell boundary and disappears when the adhesive contact is removed from the cell–cell boundary. Therefore, adhesion strength between cells depends on the geometry of the cell–cell boundary.

The force energy E_{f} due to the growth forces $f_{\mathrm{g}}(x)$ and protrusive migration force $f_{\mathrm{m}}(x)$ occurring in Ω can be written as

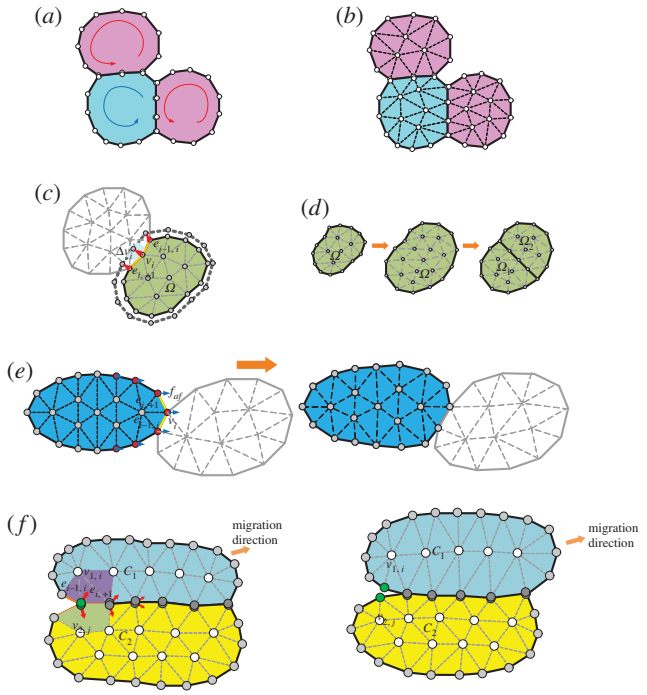

Figure 1. Geometry, discretization and dynamic changes of cells. (*a*) The boundary of each cell is defined by a anticlockwise oriented polygon containing a number of boundary vertices. (*b*) Triangular mesh tiling up each cell. (*c*) Cell growth from time t to $t + \Delta t$. The displacement vector $\Delta \boldsymbol{v}_i$ of vertex $\boldsymbol{v}_i$ after cell growth with given incremental cell volume $\Delta|\Omega|$ can be obtained by solving equations (2.3) and (2.6) that relates $\Delta \boldsymbol{v}_i$ to $\Delta|\Omega|$ through the Jacobian determinant. (*d*) When the volume of a cell Ω is doubled, cell proliferation occurs and it is then divided into two daughter cells Ω_1 and Ω_2 along the shortest axis of Ω. (*e*) Cell migration from time t to $t + \Delta t$. The protrusion force driving cell migration on each boundary vertex $\boldsymbol{v}_i$ on the leading edge is calculated, where f_{af} is the parameter of protrusion force from t to $t + \Delta t$. (*f*) Contraction forces (in red) resulting from cell elasticity are generated in response to the protrusion force on the leading edges. The attached vertices in adhesion linkage $\boldsymbol{v}_{1,j}$ and $\boldsymbol{v}_{2,j}$ (in green) from two cells in contact with one another are separated if the contraction force generated is larger than the threshold of adhesion rupture force. The purple and light green triangles are triangular elements to build sub-stiffness matrices for $\boldsymbol{v}_{1,j}$ and $\boldsymbol{v}_{2,j}$, respectively, to recover the contraction force.

$-\int_\Omega (\boldsymbol{f}_g(\boldsymbol{x}) + \boldsymbol{f}_m(\boldsymbol{x}))^{\mathrm{T}} \boldsymbol{u}(\boldsymbol{x})\,\mathrm{d}\boldsymbol{x}$. Therefore, the overall free energy E_Ω of the cell Ω can be written as

$$E_\Omega = \frac{1}{2}\int_\Omega \boldsymbol{\sigma}^{\mathrm{T}}(\boldsymbol{x})\boldsymbol{\epsilon}(\boldsymbol{x})\,\mathrm{d}\boldsymbol{x} + \frac{Y}{2}\int_\Omega u(\boldsymbol{x})^2\,\mathrm{d}\boldsymbol{x} - \int_{\partial\Omega} \sigma_a \boldsymbol{n}(\boldsymbol{x})^{\mathrm{T}}\boldsymbol{u}(\boldsymbol{x})\,\mathrm{d}\boldsymbol{x} + \sum_{\Omega\bigcap\Omega_n\neq\varnothing} \int_{\Omega\bigcap\Omega_n} f_a \boldsymbol{n}(\boldsymbol{x})^{\mathrm{T}}\boldsymbol{u}(\boldsymbol{x})\,\mathrm{d}\boldsymbol{x} - \int_\Omega (\boldsymbol{f}_g(\boldsymbol{x}) + \boldsymbol{f}_m(\boldsymbol{x}))^{\mathrm{T}}\boldsymbol{u}(\boldsymbol{x})\,\mathrm{d}\boldsymbol{x}. \tag{2.1}$$

The deformed cell reaches its balance state when the strain energy of the cell E_Ω reaches a minimum, at which we have $\partial E_\Omega(\boldsymbol{u})/\partial \boldsymbol{u} = 0$.

For each triangular element $\boldsymbol{\tau}_{i,j,k} \in T_\Omega$ of Ω, equation (2.1) can be written using the stiffness matrix method as a linear equation

$$\boldsymbol{K}_\tau \boldsymbol{u}_\tau = \boldsymbol{f}_\tau,$$

where $\boldsymbol{K}_\tau$ is the stiffness matrix of $\boldsymbol{\tau}_{i,j,k}$, $\boldsymbol{u}_\tau$ is the displacement of $\boldsymbol{\tau}_{i,j,k}$ and $\boldsymbol{f}_\tau$ is the integrated force vector on $\boldsymbol{\tau}_{i,j,k}$ (see electronic supplementary material, S1 for details of the derivation).

We then gather the element stiffness matrices of all triangular meshes in all cells and assemble them into a global stiffness matrix $\boldsymbol{K}$. The adhesion energy term in equation (2.2) contributes to $\boldsymbol{K}$ by adding a scaled identity matrix, which prevents the system of equation (2.2) from being singular. The linear relationship between the concatenated vector $\boldsymbol{u}$ of all vertices of the cells and the external force vector $\boldsymbol{f}$ on all vertices is then given by

$$\boldsymbol{K}\boldsymbol{u} = \boldsymbol{f}. \tag{2.2}$$

The behaviour of the whole collection of cells in the stationary state at a specific time step can then be obtained by solving this non-singular linear equation. For vertex v_i at $\boldsymbol{x}_i$, its new location is then updated as $\boldsymbol{x}_i' = \boldsymbol{x}_i + \boldsymbol{u}(v_i)$. As migrating cells rapidly reconstruct their cytoskeleton and adhesive structures [30], we re-calculate the triangle mesh T_Ω for each cell Ω and reset the stress to zero after location update. In our model, the time step Δt is fixed as 30 min (see electronic supplementary material, text S7 for discussion on the size of the time step).

2.1.3. Dynamic changes in cell geometry during cell growth, proliferation and migration

While the cell is moving, the positions of discretized vertices of cells change with time. We distribute forces driving cell motion onto the vertices of cells. The displacement vectors of the vertices can then be obtained by solving equation (2.2).

Cell growth. At each time interval, we consider an idealized growth force $\boldsymbol{f}_g$ that would drive a cell Ω to grow by an incremental volume $\Delta|\Omega|$, in the absence of its neighbouring cells. We assume that the direction of the growth force $\boldsymbol{f}_{g,i}$ at the boundary vertex v_i is along the direction of the normal vector $\boldsymbol{n}_i$ at v_i. We also assume that the strength $|\boldsymbol{f}_{g,i}|$ is proportional to the length of edges associated with v_i and is

$$\boldsymbol{f}_{g,i} = \gamma \frac{|\boldsymbol{e}_{i-1,i}| + |\boldsymbol{e}_{i,i+1}|}{2\sum\limits_{\boldsymbol{e}_{j,j+1}\in\partial\Omega} |\boldsymbol{e}_{j,j+1}|}\boldsymbol{n}_i, \tag{2.3}$$

where γ is a scalar. We then calculate γ by relating the volume change $\Delta|\Omega|$ and the displacement vectors $\boldsymbol{u}(\boldsymbol{x})$ at locations $\boldsymbol{x}$ through the Jacobian determinant $J(\boldsymbol{x}) = \det(\boldsymbol{F}(\boldsymbol{x}))$, where $\boldsymbol{F}(\boldsymbol{x})$ is the deformation gradient. We have

$$\begin{aligned}\Delta|\Omega| + |\Omega| &= \int_\Omega J(\boldsymbol{x})\,\mathrm{d}\boldsymbol{x} = \int_\Omega \det(\boldsymbol{F}(\boldsymbol{x}))\,\mathrm{d}\boldsymbol{x} = \int_\Omega \det\left(\boldsymbol{I} + \frac{\partial \boldsymbol{u}(\boldsymbol{x})}{\partial \boldsymbol{x}}\right)\mathrm{d}\boldsymbol{x} \\ &= \sum_{\boldsymbol{\tau}_{i,j,k}\in T_\Omega} \int_{\boldsymbol{\tau}_{i,j,k}} \det\left(\boldsymbol{I} + \frac{\partial \boldsymbol{u}(\boldsymbol{x})}{\partial \boldsymbol{x}}\right)\mathrm{d}\boldsymbol{x},\end{aligned} \tag{2.4}$$

where $\boldsymbol{I}$ is the identity matrix. $\partial \boldsymbol{u}(\boldsymbol{x})/\partial \boldsymbol{x}$ for $\boldsymbol{x} \in \boldsymbol{\tau}_{i,j,k}$ can be interpolated as $\partial \boldsymbol{u}(\boldsymbol{x})/\partial x_1 = \sum_{l\in i,j,k}(b_l/2|\boldsymbol{\tau}_{i,j,k}|)\boldsymbol{u}_l(\boldsymbol{x})$ and $\partial \boldsymbol{u}(\boldsymbol{x})/\partial x_2 = \sum_{l\in i,j,k}(c_l/2|\boldsymbol{\tau}_{i,j,k}|)\boldsymbol{u}_l(\boldsymbol{x})$, where $b_i = x_{j,2} - x_{k,2}$ and $c_i = x_{j,1} - x_{k,1}$ (see the electronic supplementary material for details). Equation (2.4) then can be written as:

$$\Delta|\Omega| + |\Omega| = \sum_{\boldsymbol{\tau}_{i,j,k}\in T_\Omega} |\boldsymbol{\tau}_{i,j,k}| \det\left(\boldsymbol{I} + \begin{pmatrix} b_i & b_j & b_k \\ c_i & c_j & c_k \end{pmatrix}(\boldsymbol{u}_i, \boldsymbol{u}_j, \boldsymbol{u}_k)^{\mathrm{T}}\right). \tag{2.5}$$

As the displacement vectors $\boldsymbol{u}_g = \{\boldsymbol{u}_1, \ldots, \boldsymbol{u}_n\}$ of vertices in cell Ω are determined by $\boldsymbol{u}_g = \boldsymbol{K}_g^{-1}\boldsymbol{f}_g$, where $\boldsymbol{K}_g$ is the stiffness matrix of Ω given by the geometry of the cell, combined with the scaled identity matrix incorporating the adhesion between the cell and the substrate and $\boldsymbol{f}_g$ is the integrated force vector of $\boldsymbol{f}_{g,i}$ given by equation (2.3). Then equation (2.5) can be rewritten as

$$\begin{aligned}\Delta|\Omega| + |\Omega| = &\sum_{\boldsymbol{\tau}_{i,j,k}\in T_\Omega} |\boldsymbol{\tau}_{i,j,k}| \\ &\times \det\left(\boldsymbol{I} + \begin{pmatrix} b_i & b_j & b_k \\ c_i & c_j & c_k \end{pmatrix}((\boldsymbol{K}_g^{-1}\boldsymbol{f}_g)_i, (\boldsymbol{K}_g^{-1}\boldsymbol{f}_g)_j, (\boldsymbol{K}_g^{-1}\boldsymbol{f}_g)_k)^{\mathrm{T}}\right).\end{aligned} \tag{2.6}$$

Then the growth force $\boldsymbol{f}_g$ that gives the incremental volume change $\Delta|\Omega|$ can be obtained by solving the coupled equations (2.3) and (2.6).

Cell proliferation. Cell proliferation occurs when the volume of the mother cell Ω is doubled. We divide Ω into two daughter cells Ω_1 and Ω_2 by adding a set of paired vertices along the shortest axis of Ω (figure 1*c*, between diagonal paired vertices).

Cell migration. To model cell migration, we distribute the protrusive migration forces f_m onto the vertices of the leading edges. Here leading edges are edges whose outward normal $\boldsymbol{n}$ and the unit vector of migration direction $\boldsymbol{v}$ has the positive inner product: $\boldsymbol{n} \cdot \boldsymbol{v} > 0$. For each boundary vertex v_i on a leading edge, the protrusive migration force $f_{m,i}$ driving v_i to migrate is calculated as

$$\boldsymbol{f}_{m,i} = \frac{1}{2} f_{af}(|\boldsymbol{e}_{i-1,i}| + |\boldsymbol{e}_{i,i+1}|)(\boldsymbol{n} \cdot \boldsymbol{v})\boldsymbol{v}, \tag{2.7}$$

where f_{af} is the parameter of protrusion force per unit length, $\boldsymbol{e}_{i-1,i}$ and $\boldsymbol{e}_{i,i+1}$ are edges connected to v_i (figure 1*e*).

2.2. Cell–cell adhesion and its rupture

Here we implicitly model cell–cell adhesions as adhesion linkages between two attached vertices from two neighbouring cells. Cell–cell adhesion occurs if the bodies of two cells would otherwise overlap. The attachment of adhesion linkage is added to each pair of vertices on the contacting surfaces, and the overlap is repaired by the *Cell-merge* primitive. The adhesion linkage then generates adhesion force f_a on the pair of attached vertices as shown in equation (2.1). In response to the protrusive migration force on the leading edges of a migrating cell, elastic force in the opposite direction occurs at the rear edges of the cell, which arises strictly from cell elasticity in our model. Once this elastic force exerted on an adhesive linkage between two vertices on two contacting cells surpasses a threshold f_θ of rupture force, the adhesion linkage between these vertices is severed.

We compute this elastic force at each vertex in the contacting surface of a cell with its neighbours in response to cell motion. For vertex $v_{1,i}$ from cell Ω_1 on the contacting surface with cell Ω_2, we can recover this elastic force vector using the sub-stiffness matrix associated with $v_{1,i}$ (figure 1*f*):

$$\boldsymbol{f}_{1,i} = \boldsymbol{K}_{1,i}\boldsymbol{u}_{1,i}, \tag{2.8}$$

where $\boldsymbol{K}_{1,i}$ is the sub-stiffness matrix constructed using the set of triangles, namely, $T_{v_{1,i}} \equiv \cup_{v_{1,i} \in \tau_k} \tau_k$, where each triangle $\tau_k \in \Omega_1$ contains vertex $v_{1,i}$ (purple triangles in figure 1*f*). Here $\boldsymbol{u}_{1,i}$ is the displacement vector, which includes the displacement of vertex $v_{1,i}$ and displacements of all of its surrounding vertices contained in $T_{v_{1,i}}$. Currently, we do not consider additional active contractile processes when calculating forces for cell rupture. Therefore, $\boldsymbol{u}_{1,i}$ here is calculated using an adapted free energy excluding the contractile energy $-\int_\Omega (\sigma_a, \sigma_a, 0)\boldsymbol{\epsilon}(\boldsymbol{x})\,\mathrm{d}\boldsymbol{x}$. For vertex $v_{2,j}$ on cell Ω_2 attached to Ω_1, we recover the elastic force similarly. If $\max(|\boldsymbol{f}_{1,i} \cdot \boldsymbol{n}_{1,i}|, |\boldsymbol{f}_{2,j} \cdot \boldsymbol{n}_{2,j}|) > f_\theta \cdot l$, where $\boldsymbol{n}_{1,i}$ and $\boldsymbol{n}_{2,j}$ are unit normal vectors of $v_{1,i}$ and $v_{2,j}$, we eliminate the attachment of adhesion linkage between vertices $v_{1,i}$ and $v_{2,j}$ (figure 1*f*). Here f_θ is the rupture force threshold per unit length, l is the half-length of the shared edge(s) between $v_{1,i}$ and $v_{2,j}$.

2.3. Primitives for topologic and geometric changes

Here we use five primitives to model topologic and geometric changes for cells undergoing movement:

— P1. *Cell-merge*: The intersecting surfaces of two colliding cells are identified and then replaced by contacting surfaces. Cell–cell adhesion is then added to each pair of attached vertices on the contacting surfaces (figure 2*a*).
— P2. *Cell-separation*: The kinematic attachment of an adhesion linkage between a pair of attached vertices is then removed when it experiences contraction force larger than the threshold (figure 2*b*).
— P3. *Edge-subdivision*: An edge longer than the threshold is then subdivided into two edges (figure 2*c*).
— P4. *Edge-simplification*: An edge shorter than the threshold is then removed (figure 2*d*).
— P5. *Sliver-removal*: A skinny triangle with an angle smaller than the threshold appears is then removed (figure 2*e*).

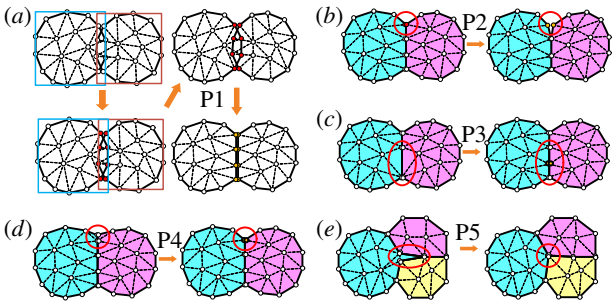

Figure 2. Primitives for cell geometric and topologic changes. (*a*) P1. *Cell-merge*: The overlapping surfaces (red vertices) of the two colliding cells are detected by examining the intersection of their bounding boxes and then repaired. (*b*) P2. *Cell-separation*: previously attached vertices on the contact surfaces of two different cells are separated from each other. (*c*) P3. *Edge-subdivision*: an edge longer than the threshold is subdivided into two edges. (*d*) P4. *Edge-simplification*: an edge shorter than the threshold is removed. (*e*) P5. *Sliver-removal*: a skinny triangle with an angle smaller than the threshold is removed.

These primitives can exhaust all possible topologic changes of cells. In addition to the cell topologic change, it is also important to detect collisions of colliding cells. Details on implementation of collision detection and realization of topologic change using these primitives can be found in electronic supplementary material, text S2.

2.4. Model of wound tissue and re-epithelialization

2.4.1. Geometry of wound bed and tissue regions

We use a simplified wound tissue to study the re-epithelialization process (figure 3*a*). In our model, wound tissue is composed of keratinocyte cells and wound elements. The wound elements include both fibrin clots and fibroblasts, with the elastic property of the wound element determined mostly by the fibrin clot, the major component of the wound site [31] (see electronic supplementary material, table S2 for the parameter values of cell and element elasticity). The combination of all wound elements is called the wound bed. The wound bed size is set to $800 \times 300\ \mu m$ (figure 3*a*) in our model. We follow a previous study [32] and divide the locations of keratinocytes into four regions according to their distance to the wound edge: Regions I, II, III, and IV have distance 0–80 μm, 80–160 μm, 160–240 μm and greater than 240 μm to the wound edge, respectively (figure 3*a*). Results reported here were obtained using this model wound tissue consisting of 8741/929 cells/wound elements and 3×10^5 vertices at the end of simulation. With a Pentium Dual CPU of 1.60 GHz and 4.00 GB RAM, each time step can be simulated in about 12 s.

2.4.2. Intracellular signalling network

During the re-epithelialization process, keratinocyte proliferation and migration are known to be controlled by an intracellular signalling network [26]. We use a simplified network taken from

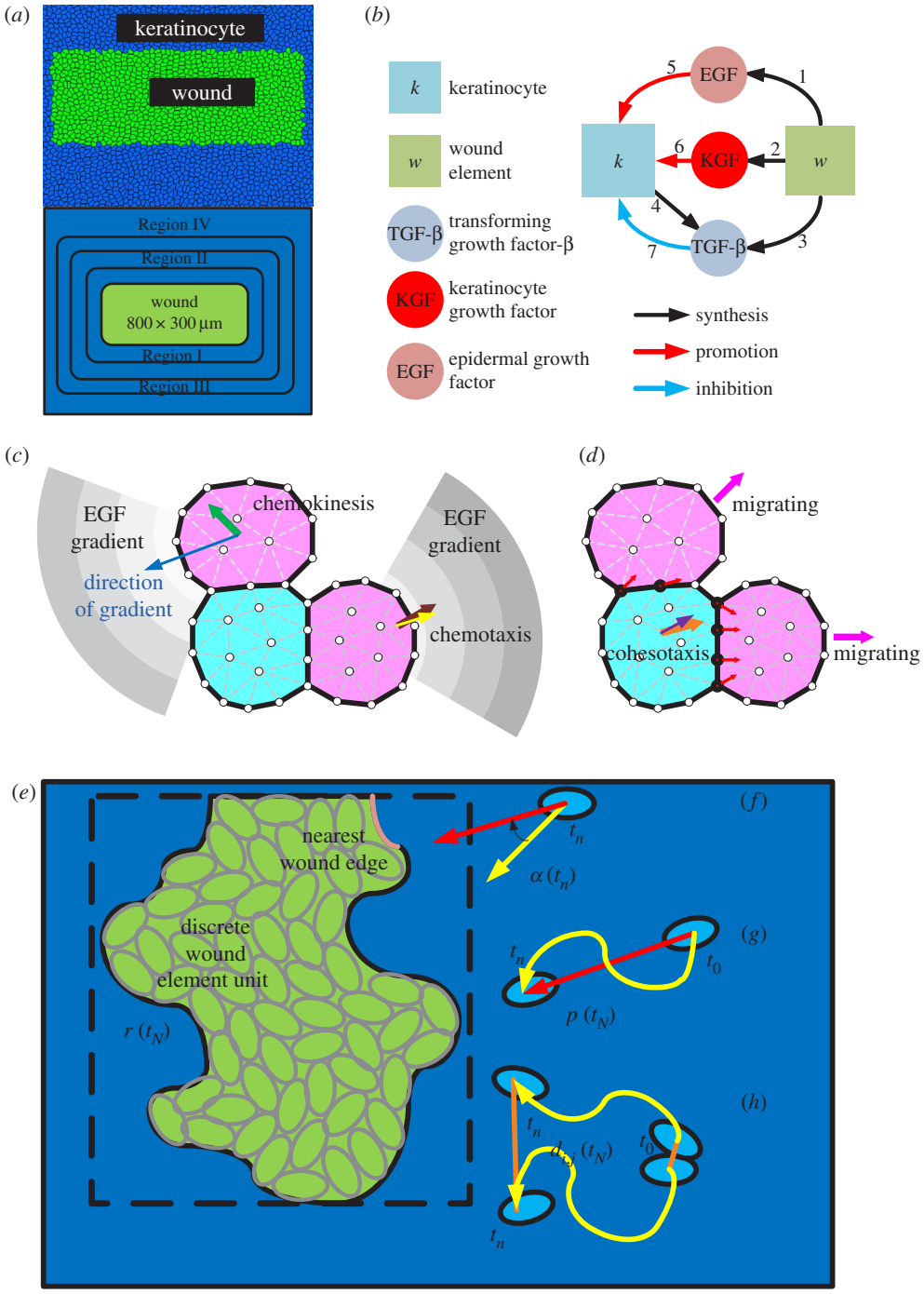

Figure 3. Model of wound tissue and re-epithelialization. (*a*) Top view of the skin wound tissue. Blue: keratinocytes; green: wound element. The size of the wound bed: 800 × 300 μm. The locations of keratinocytes are divided into four regions according to their distances to the wound edge: Regions I: 0–80 μm, II: 80–160 μm, III: 160–240 μm and IV: greater 240 μm. (*b*) Schematic of the intracellular signalling network. The synthesis and regulation relationship between the cell elements and the growth factors are represented by arrows. Detailed relationships are listed in electronic supplementary material, table S1. (*c*) In chemokinesis, the growth factor gradient (blue arrow) activates cell migration but cells move in random directions (green arrow). In chemotaxis, the migration direction is taken as the largest growth factor gradient (brown arrow), plus a random deviating angle sampled from the normal distribution of $\mathcal{N}(0, 33)$ of angles (yellow arrow). (*d*) In cohesotaxis, a cell migrates along the direction of the vectors of local intercellular elastic force. The elastic force vectors (red arrows) on each vertex (red vertices) of the cell boundary with a neighbouring cell are summed, and the overall vector (orange arrow), plus a random deviating vector whose angle is sampled from the normal distribution $\mathcal{N}(0, 33)$ of angles (purple arrow), gives the migration direction. (*e*) Wound closure ratio $r(t_N)$ is given by the number of remaining discrete wound element units in the wound bed at time t_N divided by the total number of discrete wound element units before re-epithelialization. (*f*) Migration direction angle $\alpha(t_n)$ is the angle between the direction of migration (yellow arrow) and the direction of the cell to the nearest wound edge (red arrow). (*g*) Migration persistence $p(t_N)$ is the ratio of the distance from the current position of the cell at time t_N to its original position (red line segment), divided by the length of the traversed path (yellow curve). (*h*) Normalized pair separation distance $d_{i,j}(t_N)$ is the separation distance between a pair of cells at time t_N which were initially neighbours (orange line), normalized by the average length of cell traversed path (yellow curve).

Menon *et al.* [33] (figure 3*b*) involving three growth factors, namely, keratinocyte growth factor (KGF), epidermal growth factor (EGF) and the transforming growth factor-β (TGF-β), which are known to be the most important growth factors for the re-epithelialization process [26] (see electronic supplementary material, table S1 for details).

Diffusion, synthesis and degradation of growth factors. Following Menon *et al.* [33], the change in local concentration y_i

of a growth factor i is determined by its diffusion, synthesis and degradation:

$$\frac{\partial \boldsymbol{y}_i}{\partial t} = D_i \Delta \boldsymbol{y}_i + \lambda_{s,i} - \lambda_{d,i} \boldsymbol{y}_i, \tag{2.9}$$

where D_i is the diffusion coefficient of $\boldsymbol{y}_i$, $\lambda_{s,i}$ is the synthesis rate of $\boldsymbol{y}_i$ and $\lambda_{d,i}$ is its degradation rate (see electronic supplementary material, table S2 for coefficient values). Details of the discretization of the diffusion equation can be found in our model in electronic supplementary material, text S3.

2.4.3. Cell behaviours during re-epithelialization

In our simplified model, keratinocytes can proliferate, migrate, apoptosize or become quiescent. This is controlled by a minimalistic network consisting of three growth factors (KGF, EGF and TGF-β, figure 3*b*). At a particular time step, the ith behaviour is stochastically chosen with probability

$$\pi_i = \frac{B_i}{\sum_k B_k}, \tag{2.10}$$

where $i = 1,2,3$ and 4 stands for proliferation, migration, apoptosis and quiescence, respectively. Following Menon *et al.* [33], the value of B_1 for proliferation is set to $B_1 = \alpha_1((1 + \beta_{1,\mathrm{EGF}} d_{\mathrm{EGF}})(1 + \beta_{1,\mathrm{KGF}} d_{\mathrm{KGF}})/(1 + \beta_{1,\mathrm{TGF}-\beta} d_{\mathrm{TGF}_\beta}))$, where α_1 is a scaling factor, $\beta_{1,j}$ is the coefficient for factor j, and d_j is its concentration density. The value of B_2 for migration is set to $B_2 = \alpha_2(1 + \beta_{1,\mathrm{EGF}} d_{\mathrm{EGF}})$. We also set $B_3 = \alpha_3$ for apoptosis and $B_4 = \alpha_4$ for quiescence (see electronic supplementary material, table S3 for coefficient values). In this model, elevated EGF and KGF would both increase the proportion of cells that proliferate, while elevated TGF-β would reduce proliferation.

2.4.4. Guidance mechanisms of cell migration

Cell migration is usually triggered by a directional cue from the environment. Experimental studies revealed that there exist three guidance mechanisms to determine migrating direction of a cell. Under *chemokinesis*, biochemical soluble factors stimulate a cell and initiate migration, but do not provide the direction of migration [34]. Under *chemotaxis*, the direction of cell migration is dictated by the biochemical gradient of soluble factors [34]. Under *cohesotaxis*, the direction of cell migration is determined by the intercellular force gradients [35]. While all these different guidance mechanisms may contribute to the complex process of collective cell migration, the exact roles of each individual control mechanism in regulating behaviours of cells during collective cell migration is not well understood. In our study, we assume that EGF is the trigging molecule for cell migration under both chemokinesis and chemotaxis for simplicity. Under chemokinesis, a keratinocyte begins to migrate upon activation triggered by a local EGF gradient between this cell and any of its neighbours. The direction of migration is randomly chosen from a uniform distribution $\mathcal{U}(0, 360)$ of angles. Under chemotaxis, a keratinocyte begins to migrate if there exists a local EGF gradient between a cell and any of its neighbouring cells. The migrating direction is chosen along that of the highest EGF gradient, plus a random deviation angle sampled from a normal distribution $\mathcal{N}(0, 33)$ of angles [36] (figure 3*c*). Under cohesotaxis, a keratinocyte begins to migrate if there exists local elastic force with its neighbouring cells. The migrating direction is along the vector sum of the elastic force from its neighbours, plus a random deviation angle sampled from a normal distribution $\mathcal{N}(0, 33)$ of angles (figure 3*d*).

2.4.5. Measurements of re-epithelialization and cell migration

Measuring the re-epithelialization rate. We introduce a new measure called *wound closure* $r(t_N)$ to quantify the re-epithelialization rate:

$$r(t_N) = \frac{n_{\mathrm{w}}(t_0) - n_{\mathrm{w}}(t_N)}{n_{\mathrm{w}}(t_0)}, \tag{2.11}$$

where $n_{\mathrm{w}}(t_n)$ is the number of remaining discrete wound element units in the wound bed at time t_N, $n_{\mathrm{w}}(t_0)$ is the total number of discrete wound element units in the wound bed before re-epithelialization (figure 3*e*). Initially, $r(t_0) = 0$. When re-epithelialization is completed, $r(t_N) = 1$.

Measuring collective cell migration during re-epithelialization. We introduce a new measure, *migration direction angle* $\alpha(t_n)$, to specify the direction of cell migration. It is used along with *migration persistence* $p(t_N)$ and *normalized separation distance* $d_{i,j}(t_N)$ introduced in a previous study [32].

The *migration direction angle* $\alpha(t_n)$ measures the angle between the direction of a migrating cell and its direction to the nearest wound edge at time t_n (figure 3*f*):

$$\alpha(t_n) = \arccos(\boldsymbol{u}_{\mathrm{c}} \cdot \boldsymbol{u}_{\mathrm{w}}) \cdot \mathrm{sgn}(\| \boldsymbol{u}_{\mathrm{c}} \times \boldsymbol{u}_{\mathrm{w}} \|), \tag{2.12}$$

where $\boldsymbol{u}_{\mathrm{c}}$ is the unit vector of the direction of cell migration, $\boldsymbol{u}_{\mathrm{w}}$ is the unit vector of direction from the cell mass centre to its nearest wound edge, $\mathrm{sgn}(x)$ is the sign of x (figure 3*f*). The smaller $\alpha(t_n)$ is, the more accurate the migration direction is.

Migration persistence $p(t_N)$ measures the ratio of the distance between the start and the endpoints over the length of the traversed path at time t_N [32] (figure 3*g*):

$$p(t_N) = \frac{|\boldsymbol{x}(t_N) - \boldsymbol{x}(t_0)|}{\sum_{k=0}^{N-1} |\boldsymbol{x}(t_{k+1}) - \boldsymbol{x}(t_k)|}, \tag{2.13}$$

where t_0 is the initial time, $\boldsymbol{x}(t_i)$ is the position of the cell at time step t_i. The larger $p(t_n)$ is, the more persistent the cell migration is.

The *normalized separation distance* $d_{i,j}(t_N)$ between (i,j)-cell pair measures the diverging distance of the initially neighbouring cell pair (i,j) at time t_N [32] (figure 3*h*):

$$d_{i,j}(t_N) = \frac{\|\boldsymbol{x}_i(t_N) - \boldsymbol{x}_j(t_N)| - |\boldsymbol{x}_i(t_0) - \boldsymbol{x}_j(t_0)\|}{(1/2)(\sum_{k=0}^{N-1} |\boldsymbol{x}_i(t_{k+1}) - \boldsymbol{x}_i(t_k)| + \sum_{k=0}^{N-1} |\boldsymbol{x}_j(t_{k+1}) - \boldsymbol{x}_j(t_k)|)}. \tag{2.14}$$

The numerator measures the separation distance between cells i and j at time t_N, and the denominator measures the averaged path length of cells i and j at time t_N. The smaller $d_{i,j}(t_N)$ is, the better collective cell–cell coordination for this pair of cells is during cell migration.

3. Results

3.1. Patterns of collective cell migration under different guidance mechanisms of cell migration

Biochemical and mechanical cues play important roles in guiding cell migration, but how cells respond to these cues and navigate in a dynamically changing and noisy environment remains a puzzling question [35]. We first compare the patterns of cell migration under the three different guidance mechanisms of cell migration. We characterize the patterns by quantifying the direction angle $\alpha(t_n)$, the migration persistence $p(t_N)$, and the separation distance $d_{i,j}(t_N)$ of cell migration. In our model, the biochemical cue under both chemotaxis and chemokinesis is provided by the signalling of EGF synthesized from the wound elements and transmitted into keratinocytes through diffusion. Owing to the limited ranges of diffusion, the EGF signal can reach only Regions I and II (see electronic supplementary material, figure S1). Therefore, migrating cells triggered by the EGF signal under both chemotaxis and chemokinesis were only observed in Regions I and II. For both chemotaxis and chemokinesis, $p(t_N)$ and $d_{i,j}(t_N)$ are only measured in these two regions.

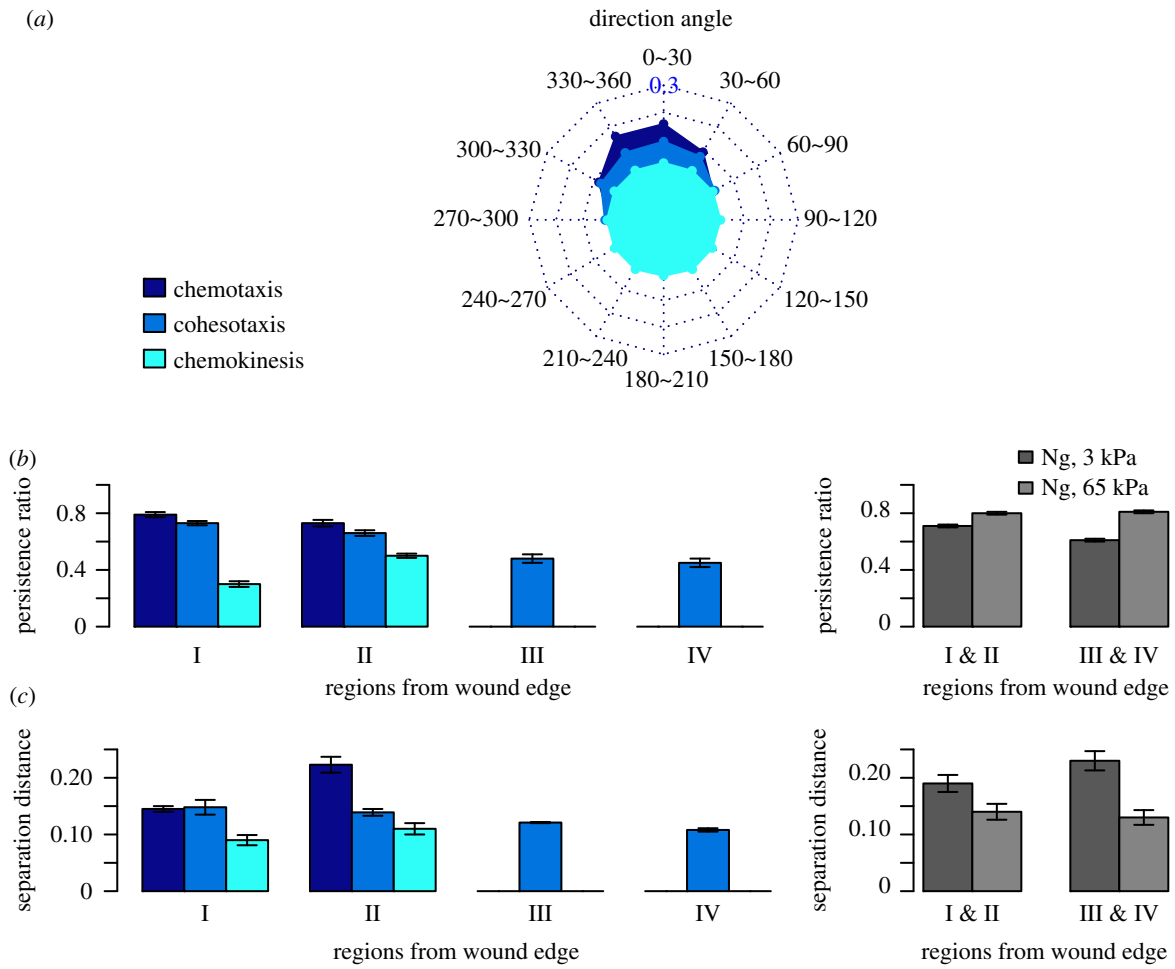

Figure 4. Cell migration directionality, persistence and separation distance under different guidance mechanisms. (*a*) Radar chart of the distribution of direction angle of migrating keratinocyte $\alpha(t_n)$ accumulated during re-epithelialization. The complete angle range (0°, 360°) is divided into 12 intervals. Each spoke of the radar chart shows the proportion of $\alpha(t_n)$ within that specific interval. (*b*,*c*) The persistence ratio $p(t_N)$ and the normalized cell separation distance $d_{i,j}(t_N)$ of migrating keratinocytes under the three guidance mechanisms in regions at varying distances from the wound edge: Regions I: 0–80 µm, II: 80–160 µm, III: 160–240 µm and IV: greater than 240 µm. Data regarding migration persistence and the normalized separation distance from the *in vitro* study of Ng *et al.* [32] using a matrix of different stiffness (3 and 65 kPa) are also plotted. The error bars depict the standard deviations of three simulation runs. The *p*-values from the *t*-tests on the simulation results of $\alpha(t_n)$, $p(t_N)$ and $d_{i,j}(t_N)$ are 9.7×10^{-5}, 5.3×10^{-5} and 1.6×10^{-3}, respectively. (Online version in colour.)

3.1.1. Biochemical cues increase the directional accuracy of cell migration

We examined the direction angle $\alpha(t_n)$ of cell migration under different guidance mechanisms to assess directional accuracy. The larger the fractions of cells with $\alpha(t_n) \leq 30^\circ$ and with $\alpha(t_n) \leq 60^\circ$ (figure 4*a*) are, the more accurate the directionality of cell migration is. Cells under chemotaxis achieved the most accurate directionality: $40 \pm 1\%$ and $68 \pm 3\%$ of the total migrating cells had $\alpha(t_n) \leq 30^\circ$ and $\alpha(t_n) \leq 60^\circ$, respectively (figure 4*a*). Cells under cohesotaxis have less accurate directionality: $28 \pm 2\%$ and $51 \pm 3\%$ of the total migrating keratinocytes had $\alpha(t_n) \leq 30^\circ$ and $\alpha(t_n) \leq 60^\circ$, respectively (figure 4*a*). As expected, cells under chemokinesis migrated in random direction, with only $16 \pm 1\%$, and $33 \pm 1\%$ of the total migrating cells with $\alpha(t_n) \leq 30^\circ$ and $\alpha(t_n) \leq 60^\circ$, respectively, both at the levels expected for random directionality distributed uniformly between 0° and 360° (figure 4*a*). Overall, cells under guidance of the biochemical cue migrated with much better directionality.

3.1.2. Biochemical cues increase cell migration persistence

We then examined the migration persistence $p(t_N)$ of cells under different guidance mechanisms. Cells with larger $p(t_N)$ have higher persistent migration. Under both chemotaxis and cohesotaxis, cells close to the wound edge migrated with higher persistence than cells far from the wound edge. Under chemotaxis, the persistences decreased slightly from $p(t_N) = 79 \pm 1\%$ in Region I to $p(t_N) = 73 \pm 1\%$ in Region II, with the overall high persistence ($p(t_N) > 70\%$) maintained throughout Regions I and II where biochemical signals were present (figure 4*b*). Under cohesotaxis, the persistence decreased from $p(t_N) = 73 \pm 2\%$ in Region I to $p(t_N) = 66 \pm 2\%$ in Region II, and then decreased significantly to only $p(t_N) = 45 \pm 3\%$ in Region IV, as the distance of cells from the wound edge increased (figure 4*b*). Chemokinesis differed from both chemotaxis and cohesotaxis, as cells migrated with very low persistence ($p(t_N) \leq 50\%$ in both Region I and Region II) because of the random nature of the migrating direction (figure 4*b*). The value of $p(t_N)$ measured from the *in vitro* study of Ng *et al.* [32] is also plotted to show that our simulation results are in the same order of magnitude (figure 4*b*). Overall, cells under guidance of the biochemical cue migrated with the highest persistence.

3.1.3. Mechanical cues improve coordination of collective cell migration

We then measured the normalized cell pair separation distance $d_{i,j}(t_N)$ under different guidance mechanisms. Better

collective cell migration has smaller $d_{i,j}(t_N)$. Under both chemotaxis and chemokinesis, $d_{i,j}(t_N)$ became larger as the distance to the wound edge increased. Under chemotaxis, the separation distance $d_{i,j}(t_N)$ increased significantly from 0.14 ± 0.01 in Region I to 0.22 ± 0.01 in Region II (figure 4*c*). Under chemokinesis, $d_{i,j}(t_N)$ increased slightly from 0.08 ± 0.01 in Region I to 0.10 ± 0.01 in Region II (figure 4*c*). However, under cohesotaxis the separation distance decreased as the distance from the wound edge increased: $d_{i,j}(t_N)$ decreased from 0.15 ± 0.01 in Region I to 0.11 ± 0.01 in Region IV (figure 4*c*). Our simulation results are in general agreement with experiments of Ng *et al.* [32] (figure 4*c*). These results demonstrated that mechanical cues can coordinate collective cell migration better, with lower separation distance between migrating cell pairs.

3.2. Spatio-temporal patterns of cell proliferation under biochemical and mechanical cues

Cell proliferation is fundamental to many essential cellular physiological processes. It is regulated by chemical signals and mechanical stimuli [37]. In addition, the proliferation of individual cells is also influenced by its neighbouring cells. A previous study reported that contact inhibition of cell movement affects cell growth rates during tissue development [37]. Therefore, characterizing and modelling of cell proliferation also requires consideration of the effects of other cells, including those that may be in migration.

In this section, we examine through simulation how specific patterns of cell proliferation in a population of cells arise under different guidance mechanisms of biochemical and mechanical cues. We divided the whole tissue of size 1600×700 µm into 56 blocks, each of size 200×100 µm. Blocks directly covering the wound bed belong to the *central region* (12 blocks); blocks immediately neighbouring the wound bed belong to the *surrounding region* (18 blocks). The time-course of re-epithelialization is divided into four intervals, namely, 0–12, 13–24, 25–36 and 37–48 h, after the initiation of re-epithelialization. The proliferation index of keratinocyte $\rho_i(j)$ in region i at time interval j is then calculated as $\rho_i(j) = n_{d,i}(j)/n_i(j)$, where $n_{d,i}(j)$ is the number of dividing keratinocytes that generate new cells inside region i during time interval j, $n_i(j)$ is the average number of keratinocytes inside region i during time interval j.

The spatial pattern of distribution of proliferating keratinocytes differs in tissue under chemotaxis and tissue under cohesotaxis (figure 5*a*,*b*). Under chemotaxis, proliferating keratinocytes were highly concentrated in the region surrounding the wound (figure 5*a*), but were more scattered throughout the tissue under cohesotaxis (figure 5*b*). Compared with cohesotaxis, the spatial proliferating pattern under chemotaxis exhibits a burst of cell proliferation at the wound margin during re-epithelialization. This is similar to a previous experimental study [38].

The spatio-temporal patterns of the proliferation in figure 5 also demonstrate the effects of contact inhibition. In our model, cell growth is inhibited due to volume exclusion if a cell is in contact with the surrounding cells. When cells migrate, such inhibition is relieved. Under biochemical cues, there is far less cell proliferation in the distant regions (figure 5*a*), as cell migration occurs only in regions close to the wound bed. By contrast, proliferating cells are more evenly distributed under mechanical cues, where cell migration occurs in all regions across the wound tissue (figure 5*b*).

In addition, the temporal patterns of keratinocyte proliferation also differ under chemotaxis and cohesotaxis (figure 5*c*,*d*). Under chemotaxis, the proliferation index $\rho_i(j)$ in the central region remained at an elevated level after 24 h but decreased significantly in the surrounding region after 24 h (figure 5*c*). $\rho_i(j)$ in the central region reached $21.4 \pm 1.1\%$ during the first 24 h and remained as $24.6 \pm 1.0\%$ after 24 h. $\rho_i(j)$ in the surrounding region reached $14.8 \pm 0.9\%$ during the first 24 h, but decreased to $8.7 \pm 1.0\%$ after 24 h. Under cohesotaxis, the proliferation index $\rho_i(j)$ in both the central and surrounding regions had similar patterns (figure 5*d*). $\rho_i(j)$ in the central region increased from $5.2 \pm 0.2\%$ to $19.2 \pm 1.0\%$ in the first 24 h, and then decreased to $16.2 \pm 0.6\%$ after 24 h. $\rho_i(j)$ in the surrounding region increased from $1.0 \pm 0.1\%$ to $13.1 \pm 0.8\%$ in the first 24 h, and then decreased to $9.1 \pm 0.6\%$ after 24 h. These temporal patterns of proliferation were also maintained at an accelerated proliferation level (modelled by decreasing the synthesis rate of TGF-β), and at inhibited proliferation level (modelled by increasing the synthesis rate of TGF-β) under either chemotaxis (figure 5*e*,*g*) or cohesotaxis (figure 5*f*,*h*).

The temporal pattern of keratinocyte proliferation under chemotaxis showed that the proliferation index in the central wound region remained at a high level, while proliferation in the surrounding region decreased significantly (figure 5*c*). This is similar to the results of a recent experimental study [39].

Overall, our simulation using a simplified re-epithelialization model suggests that different guidance cues may influence the pattern of cell proliferation. The general agreement between our simulation results and experimental observations raise the possibility that biochemical cues are likely the dominant factors influencing the migration of keratinocytes in the region surrounding a wound.

3.3. Effects of different guidance mechanisms on the re-epithelialization timeline and cell migration speed

Timely re-epithelialization is important for tissue regeneration, as chronic re-epithelialization may lead to fatal illness such as organ fibrosis and carcinogenesis [40]. In previous sections, we compared measurements of cell migration (e.g. $\alpha(t_n)$, $p(t_N)$ and $d_{i,j}(t_N)$) and cell proliferation (e.g. $\rho_i(j)$) at the cell level under different guidance mechanisms. Here we compare the process of overall re-epithelialization at the tissue level by examining how different guidance mechanisms influence the timeline of re-epithelialization. Experimental study on normal re-epithelialization showed that the wound closure rate is around $300\ \mu m\ d^{-1}$ [39]. It would take 24∼48 h to achieve complete wound closure for the wound size we used. In our simulation, the time duration for full wound closure, namely when the wound closure ratio $r(t_N)$ increased from 0.0 to 1.0, was 57 ± 1 h for chemotaxis, 52 ± 1 h for cohesotaxis and 186 ± 4 h for chemokinesis (figure 6*a*–*c*; see electronic supplementary material, videos S1–3). The wound closure time for both chemotaxis and cohesotaxis were within the range of physiological time as measured in [39] and the progression of wound closure ratio is also similar to the results from an *in vitro* study [39] (more details are available in electronic supplementary material, text S6). But the wound closure time was four to five times longer than the observed physiological time under chemokinesis (figure 7*a*).

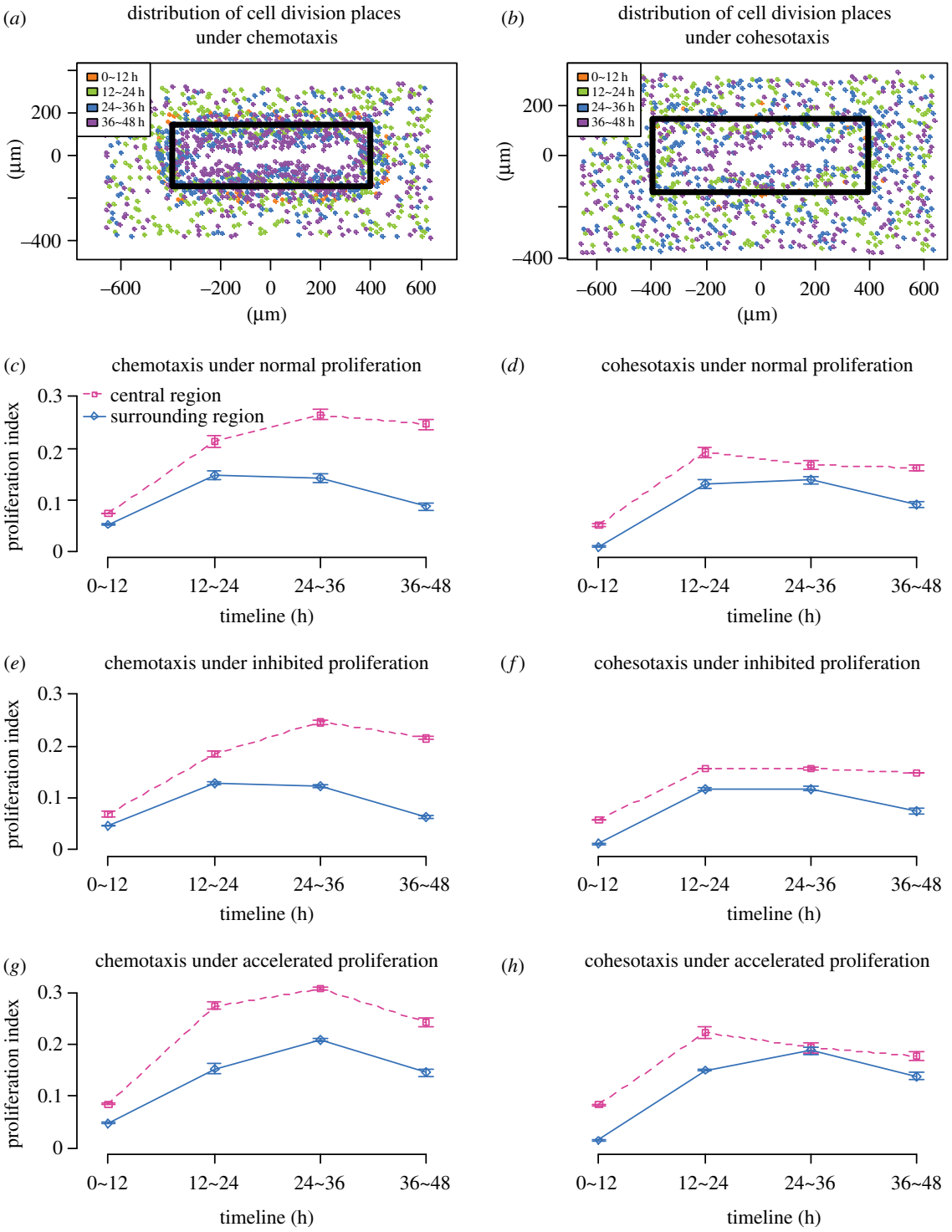

Figure 5. Spatio-temporal patterns of keratinocyte proliferation under biochemical and mechanical cues. (*a*,*b*) Distributions of dividing keratinocytes under biochemical cue (chemotaxis) and mechanical cue (cohesotaxis). Dividing cells are coloured according to division time. Orange: 0–12 h, green: 12–24 h, blue: 24–36 h and purple: 36–48 h. Black box indicates the initial wound edge. (*c*,*e*,*g*) The proliferation index $\rho_i(j)$ of the central region and the surrounding region over time under chemotaxis, with normal, inhibited (3 × synthesis rate of TGF-β), and accelerated keratinocyte proliferation (0.3 × synthesis rate of TGF-β), respectively. (*d*,*f*,*h*) The keratinocyte proliferation index $\rho_i(j)$ of the central region and the surrounding region over time under cohesotaxis, with normal, inhibited (3 × synthesis rate of TGF-β), and accelerated keratinocyte proliferation (0.3 × synthesis rate of TGF-β), respectively. The error bars depict the standard deviations of three simulation runs.

These results indicated that directional cues to guide cell migration is necessary for timely wound closure.

We also measured the migration speed $s(t_N)$, which is defined as the total length of the migrating trajectory over migrating time. Cells under cohesotaxis exhibited the highest migration speed in Region I, with $s(t_N) = 3.4 \pm 0.1\ \mu m\ h^{-1}$. By contrast, the migration speed under chemotaxis in Region I was only $s(t_N) = 2.8 \pm 0.1\ \mu m\ h^{-1}$. Under both chemotaxis and cohesotaxis, the migration speed in Region I is comparable with the physiological range of the observed speed of single keratinocyte migration of $\sim 5\ \mu m\ h^{-1}$ [41,42]. Under chemokinesis, however, the migration speed was only $s(t_N) = 0.9 \pm 0.1\ \mu m\ h^{-1}$, which was much slower than that of other mechanisms with guidance of a directional cue (figure 7*b*).

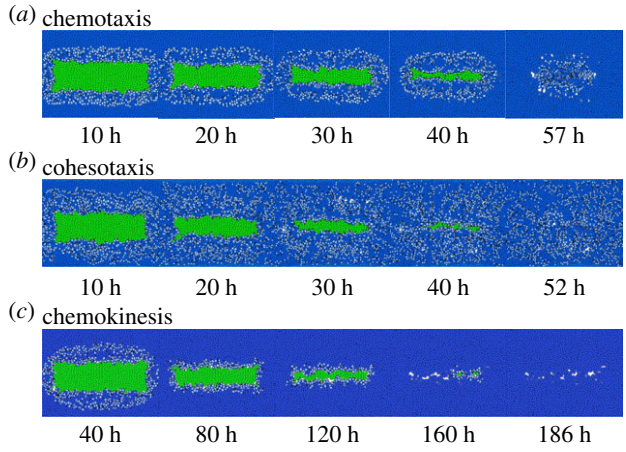

Figure 6. Snapshots of wound tissue under different guidance mechanisms of cell migration. (*a–c*) Snapshots of tissue during re-epithelialization under the three different guidance mechanisms. Blue: keratinocytes; green: wound elements and light blue: migrating keratinocytes.

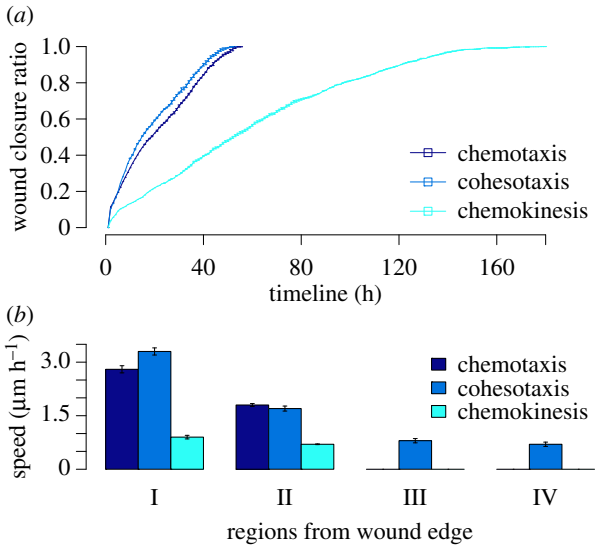

Figure 7. Re-epithelialization rate and cell migration speed under different guidance mechanisms. (*a*) Wound closure ratio $r(t_N)$ over time under the three different guidance mechanisms. (*b*) Average migration speed $s(t_N)$ of keratinocytes during re-epithelialization in regions at varying distances from the wound edge: Regions I: 0–80 μm, II: 80–160 μm, III: 160–240 μm, IV: greater than 240 μm. The error bars depict the standard deviations of three simulation runs.

These results indicate that directional cues to guide cell migration are essential for wound tissue to achieve the rapid cell migration that is necessary for in-time re-epithelialization.

4. Discussion

In this study, we developed a novel computational model called DyCelFEM. It accounts for detailed changes in cellular shapes and mechanics of a large population of interacting cells. It can model the full range of cell motion, from free movement of individual cells to large scale collective cell migration. Furthermore, the transmission of mechanical forces via intercellular adhesion and its rupture is also modelled. In addition, our preliminary results suggest that an accurate account of cell morphology such as changes of cell–cell boundaries is important for timely re-epithelialization (data not shown). With the intracellular protein signalling networks embedded in individual cells, biochemical control of cell behaviours can also be modelled. Overall, the DyCelFEM model can be used to study biological processes involving 10^{3-4} of migrating cells subject to dynamic changes in shape and mechanics.

We applied the DyCelFEM method to examine the effects of biochemical and mechanical cues in regulating cell migration and in controlling tissue patterning during the re-epithelialization process using a simplified wound tissue model. Our results show that biochemical cues have local influence over the tissue (figure 6*a*), while mechanical cues have more global impact on the tissue. This is similar to observations from a previous study where the migrating cue taken from the intercellular force regulated by merlin protein showed long-distance influence on the cells [43]. In addition, biochemical cues are better at guiding cell migration with improved directionality and higher persistence (figure 4*a*,*b*), while mechanical cues are better at coordinating collective migration of cells (figure 4*c*). Based on comparison with *in vitro* studies [38,39], our results suggest that biochemical cues likely play dominant roles in guiding the migration of cells located in the regions surrounding wounds.

A previous study has also shown that small wounds can be closed without cell proliferation [44]. This can be simulated by setting α_1 in equation (2.10) to zero. Our results showed that under non-proliferative conditions, wound closure with both chemotaxis and cohesotaxis cues can be faster if the proportion of migrating cells increases. However, there are large lesioned and unsealed gaps remaining upon completion of re-epithelialization, as there are insufficient fresh cells to fill the wound bed. Overall, our results suggest that cell proliferation is essential for full closure of large wounds (see electronic supplementary material, text S8 for more details).

In this study, we examined the roles of mechanical and chemical cues separately. In reality, these two types of cue are coupled and entangled, and cooperatively regulate overall cell behaviour. For example, chemotactic cues can modulates integrins and influence adhesion of cells to the substrate [45]. Adhesion to the substrate can in turn influence signalling networks, which then alter cell–cell adhesion [32]. There are examples where mechanical cues can promote the directionality and persistence of cell migration, and biochemical signalling can influence cell mechanics and the collective behaviour of cells. For example, it was reported that mechanical cues from changes in collagen topography in the ECM can improve the persistence of cancer cell migration [46]. In addition, the merlin protein can serve as a mechanochemical transducer to help coordinate collective cell migration [43]. To understand such complex phenomena, more detailed networks of paracrine signalling and feedback loops between cells and their environmental matrix need to be developed and incorporated in our model. In summary, further improvement in the DyCelFEM model, additional *in vivo* and *in silico* studies are necessary to draw further conclusions on the roles of biochemical and mechanical cues in specific *in vivo* settings.

There are a number of limitations of our wound model. First, we did not consider the purse-string mechanism of wound healing. Cell crawling and acto-myosin cable contraction in a purse-string manner are the two well-known mechanisms driving epithelial wound closure [47]. While the former plays dominant roles in the closure of small defects

(about 20 cells) [48], our study focus on closure of wounds of larger size where the mechanism of cell crawling driven by protrusion takes the dominant role [44]. Therefore, the purse-string mechanism is not considered in our current model (see more details in electronic supplementary material, text S5). Second, we did not consider realistic adhesion-coupling between cells. A possible improvement would be to model the adhesion between cells as springs with the adhesion force depending on the displacement of the two vertices of the adhesive contact. Currently, the scale of vertex displacement in our model is at the level of micrometres, which is much larger than the scale of cellular adhesion, which is usually at the level of nanometres [49]. Therefore, we simplify and treat cell–cell adhesion in our model using constant force. Third, our model is also limited as there is no feedback loops from cell–ECM interactions on cadherin-based cell–cell interactions and migration depends only on cell–cell adhesion. Although cells in counterproductive migration, where cells move away from the wound bed, are seen (figure 4*a*, intervals between 150° and 210°), neither large-scale movement nor extensive swirling are observed. However, these limitations can be removed with further development of DyCelFEM.

Authors' contributions. Conceived and designed the experiments: J.Z., Y.C., L.A.D. and J.L. Performed the experiments: J.Z. and Y.C. Analysed the data: J.Z., Y.C. and J.L. Wrote the paper: J.Z., Y.C., L.A.D. and J.L.

Competing interests. We declare we have no competing interests.

Funding. We would like to acknowledge NIH grant no. GM079804, GM50875 and NSF grant no. MCB-1415589 for financial support.

Acknowledgements. The authors thank Dr Hammad Naveed and Wei Tian for useful discussion. We thank the anonymous reviewers for very helpful suggestions.

References

1. Alberts B, Johnson A, Lewis J, Morgan D, Raff M, Roberts K, Walter P. 2008 *Molecular biology of the cell*. New York, NY: Garland.
2. Weber GF, Bjerke MA, DeSimone DW. 2012 A mechanoresponsive cadherin–keratin complex directs polarized protrusive behavior and collective cell migration. *Dev. Cell* **22**, 104–115. (doi:10.1016/j.devcel.2011.10.013)
3. Brugués A *et al.* 2014 Forces driving epithelial wound healing. *Nat. Phys.* **10**, 683–690. (doi:10.1038/nphys3040)
4. Oakes PW, Banerjee S, Marchetti CM, Gardel M. 2014 Geometry regulates traction stresses in adherent cells. *Biophys. J.* **107**, 825–833. (doi:10.1016/j.bpj.2014.06.045)
5. Arciero JC, Mi Q, Branca MF, Hackam DJ, Swigon D. 2011 Continuum model of collective cell migration in wound healing and colony expansion. *Biophys. J.* **100**, 535–543. (doi:10.1016/j.bpj.2010.11.083)
6. Lee P, Wolgemuth CW. 2011 Crawling cells can close wounds without purse strings or signaling. *PLoS Comput. Biol.* **7**, e1002007. (doi:10.1371/journal.pcbi.1002007)
7. Cochet-Escartin O, Ranft J, Silberzan P, Marcq P. 2014 Border forces and friction control epithelial closure dynamics. *Biophys. J.* **106**, 65–73. (doi:10.1016/j.bpj.2013.11.015)
8. Chen N, Glazier JA, Izaguirre JA, Alber MS. 2007 A parallel implementation of the cellular potts model for simulation of cell-based morphogenesis. *Comput. Phys. Commun.* **176**, 670–681. (doi:10.1016/j.cpc.2007.03.007)
9. Xu Z, Chen N, Kamocka M, Malgorzata M, Rosen E, Alber M. 2008 A multiscale model of thrombus development. *J. R. Soc. Interface* **5**, 705–722. (doi:10.1098/rsif.2007.1202)
10. Albert PJ, Schwarz US. 2016 Dynamics of cell ensembles on adhesive micropatterns: bridging the gap between single cell spreading and collective cell migration. *PLoS Comput. Biol.* **12**, e1004863. (doi:10.1371/journal.pcbi.1004863)
11. Nagai T, Honda H. 2009 Computer simulation of wound closure in epithelial tissues: cell–basal-lamina adhesion. *Phys. Rev. E* **80**, 061903. (doi:10.1103/physreve.80.061903)
12. Vitorino P, Hammer M, Kim J, Meyer T. 2011 A steering model of endothelial sheet migration recapitulates monolayer integrity and directed collective migration. *Mol. Cell. Biol.* **31**, 342–350. (doi:10.1128/mcb.00800-10)
13. Basan M, Elgeti J, Hannezo E, Rappel WJ, Levine H. 2013 Alignment of cellular motility forces with tissue flow as a mechanism for efficient wound healing. *Proc. Natl Acad. Sci. USA* **110**, 2452–2459. (doi:10.1073/pnas.1219937110)
14. Newman T. 2005 Multicellular systems using subcellular elements. *Math. Biosci. Eng.* **2**, 613–624.
15. Rejniak KA. 2007 An immersed boundary framework for modelling the growth of individual cells: an application to the early tumour development. *J. Theor. Biol.* **247**, 186–204. (doi:10.1016/j.jtbi.2007.02.019)
16. Hutson MS, Veldhuis J, Ma X, Lynch HE, Cranston PG, Wayne Brodland G. 2009 Combining laser microsurgery and finite element modeling to assess cell-level epithelial mechanics. *Biophys. J.* **97**, 3075–3085. (doi:10.1016/j.bpj.2009.09.034)
17. Vermolen F, Gefen A. 2015 Semi-stochastic cell-level computational modelling of cellular forces: application to contractures in burns and cyclic loading. *Biomech. Model. Mechanobiol.* **14**, 1181–1195. (doi:10.1007/s10237-015-0664-2)
18. Osborne JM, Fletcher AG, Pitt-Francis JM, Maini PK, Gavaghan DJ. 2016 Comparing individual-based approaches to modelling the self-organization of multicellular tissues. *bioRxiv*, 074351. (doi:10.1101/074351)
19. Kachalo S, Naveeed H, Cao Y, Zhao J, Liang J. 2015 Mechanical model of geometric cell and topological algorithm for cell dynamics from single-cell to formation of monolayered tissues with pattern. *PLoS ONE* **10**, e0126484. (doi:10.1371/journal.pone.0126484)
20. Li Y, Naveed H, Kachalo S, Xu LX, Liang J. 2014 Mechanisms of regulating tissue elongation in drosophila wing: Impact of oriented cell divisions, oriented mechanical forces, and reduced cell size. *PLoS ONE* **9**, e086725. (doi:10.1371/journal.pone.0086725)
21. Li Y, Naveed H, Kachalo S, Xu LX, Liang J. 2012 Mechanisms of Regulating Cell Topology in Proliferating Epithelia: Impact of Division Plane, Mechanical Forces, and Cell Memory. *PLoS ONE* **7**, e43108. (doi:10.1371/journal.pone.0043108)
22. Graner F, Glazier JA. 1992 Simulation of biological cell sorting using a two-dimensional extended potts model. *Phys. Rev. Lett.* **69**, 2013. (doi:10.1103/physrevlett.69.2013)
23. Schiff LI. 1968 *Quantum mechanics*, 3rd edn. New York, NY: M cGraw-Hill.
24. Tayllamin B, Mendez S, Moreno R, Chau M, Nicoud F. 2010 Comparison of body-fitted and immersed boundary methods for biomechanical applications. In *Proc. of the Fifth European Conf. on Computational Fluid Dynamics, ECCOMAS CFD 2010, Lisbon, Portugal, 14–17 June* (eds JCF Pereira, A Sequeira), pp. 1–20.
25. Brodland GW, Viens D, Veldhuis JH. 2007 A new cell-based FE model for the mechanics of embryonic epithelia. *Comput. Methods Biomech. Biomed. Eng.* **10**, 121–128. (doi:10.1080/10255840601124704)
26. Larjava H, Häkkinen L, Koivisto L. 2011 Re-epithelialization of wounds. *Endod. Top.* **24**, 59–93. (doi:10.1111/etp.12007)
27. Edelsbrunner H. 2001 *Geometry and topology for mesh generation*. Cambridge monographs on applied and computational mathematics. Cambridge, UK: Cambridge University Press.
28. Bonakdar N, Gerum R, Kuhn M, Sporrer M, Lippert A, Schneider W, Aifantis K, Fabry B. 2016 Mechanical plasticity of cells. *Nat. Mater.* **15**, 1090–1094. (doi:10.1038/nmat4689)

29. Dong S, Long Z, Tang L, Jiang Y, Yan Y. 2014 Simulation of growth and division of 3D cells based on finite element method. *Int. J. Appl. Mech.* **6**, 1450041. (doi:10.1142/S1758825114500410)
30. Keren K, Pincus Z, Allen GM, Barnhart EL, Marriott G, Mogilner A, Theriot JA. 2008 Mechanism of shape determination in motile cells. *Nature* **453**, 475–480. (doi:10.1038/nature06952)
31. Zielinski R, Mihai C, Kniss D, Ghadiali SN. 2013 Finite element analysis of traction force microscopy: influence of cell mechanics, adhesion, and morphology. *J. Biomech. Eng.* **135**, 071009. (doi:10.1115/1.4024467)
32. Ng MR, Besser A, Danuser G, Brugge JS. 2012 Substrate stiffness regulates cadherin-dependent collective migration through myosin-II contractility. *J. Cell Biol.* **199**, 545–563. (doi:10.1083/jcb.201207148)
33. Menon SN, Flegg JA, McCue SW, Schugart RC, Dawson RA, Sean McElwain DL. 2012 Modelling the interaction of keratinocytes and fibroblasts during normal and abnormal wound healing processes. *Proc. R. Soc. B.* **279**, 3329–3338. (doi:10.1098/rspb.2012.0319)
34. Petrie RJ, Doyle AD, Yamada KM. 2009 Random versus directionally persistent cell migration. *Nat. Rev. Mol. Cell Biol.* **10**, 538–549. (doi:10.1038/nrm2729)
35. Roca-Cusachs P, Sunyer R, Trepat X. 2013 Mechanical guidance of cell migration: lessons from chemotaxis. *Curr. Opin. Cell Biol.* **25**, 543–549. (doi:10.1016/j.ceb.2013.04.010)
36. Vedel S, Tay S, Johnston DM, Bruus H, Quake SR. 2013 Migration of cells in a social context. *Proc. Natl Acad. Sci. USA* **110**, 129–134. (doi:10.1073/pnas.1204291110)
37. Tremel A, Cai A, Tirtaatmadia N, Hughes BD, Stevens GW, Landman KA, O'Connor AJ. 2008 Cell migration and proliferation during monolayer formation and wound healing. *Chem. Eng. Sci.* **64**, 247–253. (doi:10.1016/j.ces.2008.10.008)
38. Garlick JA. 2007 Engineering skin to study human disease–tissue models for cancer biology and wound repair. In *Tissue engineering II*, pp. 207–239. Berlin, Germany: Springer.
39. Safferling K, Sütterlin T, Westphal K, Ernst C, Breuhahn K, James M, Jäger D, Halama N, Grabe N. 2013 Wound healing revised: a novel reepithelialization mechanism revealed by *in vitro* and *in silico* models. *J. Cell Biol.* **203**, 691–709. (doi:10.1083/jcb.201212020)
40. Epstein FH, Singer AJ, Clark RA. 1999 Cutaneous wound healing. *N. Engl. J. Med.* **341**, 738–746. (doi:10.1056/NEJM199909023411006)
41. Kirfel G, Rigort A, Borm B, Schulte C, Herzog V. 2003 Structural and compositional analysis of the keratinocyte migration track. *Cell Motil. Cytoskelet.* **55**, 1–13. (doi:10.1002/cm.10106)
42. Laplante AF, Germain L, Auger FA, Moulin V. 2015 Mechanisms of wound reepithelialization: hints from a tissue-engineered reconstructed skin to long-standing questions. *FASEB J.* **15**, 2377–2389. (doi:10.1096/fj.01-0250com)
43. Das T, Safferling K, Rausch S, Grabe N, Boehm H, Spatz JP. 2015 A molecular mechanotransduction pathway regulates collective migration of epithelial cells. *Nat. Cell Biol.* **17**, 276–287. (doi:10.1038/ncb3115)
44. Ravasio A *et al.* 2015 Gap geometry dictates epithelial closure efficiency. *Nat. Commun.* **6**, 7683. (doi:10.1038/ncomms8683)
45. Weber G, Bjerke MA, DeSimone DW. 2011 Integrins and cadherins join forces to form adhesive networks. *J. Cell Sci.* **124**, 1183–1193. (doi:10.1242/jcs.064618)
46. Riching K *et al.* 2014 3D collagen alignment limits protrusions to enhance breast cancer cell persistence. *Biophys. J.* **107**, 2546–2558. (doi:10.1016/j.bpj.2014.10.035)
47. Begnaud S, Chen T, Delacour D, Mege RM, Ladoux B. 2016 Mechanics of epithelial tissues during gap closure. *Curr. Opin. Cell Biol.* **42**, 52–62. (doi:10.1016/j.ceb.2016.04.006)
48. Vedula SRK *et al.* 2015 Mechanics of epithelial closure over non-adherent environments. *Nat. Commun.* **6**, 6111. (doi:10.1038/ncomms7111)
49. Hynes R. 1992 Integrins: versatility, modulation, and signaling in cell adhesion. *Cell* **69**, 11–25. (doi:10.1016/0092-8674(92)90115-S)

Supplementary Text 1

Geometry and discretization of the cell

In our model, a two-dimensional cell Ω is defined by its boundary $\partial\Omega$, which is represented by an oriented polygon connecting a set of boundary vertices $V_{\partial\Omega} \equiv \{\boldsymbol{v}_i \in \partial\Omega \subset \mathbb{R}^2\}$. The cell boundary $\partial\Omega$ is a closed chain of oriented edges $(\boldsymbol{e}_{1,2}, \boldsymbol{e}_{2,3}, \cdots, \boldsymbol{e}_{n,1})$, where edge $\boldsymbol{e}_{i,i+1}$ connects modulus n consecutive boundary vertices $\boldsymbol{v}_i$ and $\boldsymbol{v}_{i+1}$ in the counter-clock wise orientation. We denote the location of a vertex $\boldsymbol{v}_i$ as $\boldsymbol{x}_i$. In this study, a perfectly circular cell has a radius $r_\Omega = 10\ \mu m$, and $n = 20$ vertices are used to define $\partial\Omega$. This gives the default edge length $\boldsymbol{e}_{i,i+1} = 3.14\ \mu m$. We first compute the Delaunay triangulation D_Ω of the cell Ω using only boundary vertices $V_{\partial\Omega}$. We then follow the *farthest point sampling* method [1] to test if the radius of circumsphere of any triangle in D_Ω is larger than a threshold $|\boldsymbol{e}_\theta| := 3.14\ \mu m$. If so, a new vertex is inserted at the circumcenter of this triangle and D_Ω is updated, using the 1-to-3 edge flip and the 2-to-2 edge flip, upon examination of all edges in the star of the newly inserted vertex (see [2] for details). This is repeated until all new triangles have their circumsphere radius shorter than $|\boldsymbol{e}_\theta|$. The cell Ω is therefore tessellated by a set of triangles $T_\Omega = \{\boldsymbol{\tau}_{i,j,k}\}$, with vertices i, j and k of triangle $\boldsymbol{\tau}_{i,j,k}$ drawn from the set of boundary vertices $V_{\partial\Omega}$ and the set of newly inserted interior vertices $V_{\mathrm{Int}\Omega}$. The vertices $V_\Omega = V_{\partial\Omega} \cup V_{\mathrm{Int}}$, edges $E_\Omega = \{\boldsymbol{e}_{i,j} | \boldsymbol{v}_i, \boldsymbol{v}_j \in V\}$, and triangles T_Ω form a simplicial complex K_Ω.

Deformation energy of the cell

Denote the displacement of a vertex at $\boldsymbol{x}$ as $\boldsymbol{u}(\boldsymbol{x}) = (u_1(\boldsymbol{x}), u_2(\boldsymbol{x}))^T \in \mathbb{R}^2$. According to linear elastic theory, $\boldsymbol{\epsilon}(\boldsymbol{x})$ takes the form of $\epsilon_{1,1} = \partial u_1/\partial x_1$, $\epsilon_{2,2} = \partial u_2/\partial x_2$, and $\epsilon_{1,2} = \epsilon_{2,1} = \frac{1}{2}(\partial u_1/\partial x_2 + \partial u_2/\partial x_1)$. We use the stress tensor $\boldsymbol{\sigma}$ to represent the forces, which is related to the strain tensor $\boldsymbol{\epsilon}$ through the Hooke's law: $\boldsymbol{\sigma} = \boldsymbol{D}\boldsymbol{\epsilon}$, where $\boldsymbol{D} = \begin{pmatrix} \lambda+2\mu & \lambda & 0 \\ \lambda & \lambda+2\mu & 0 \\ 0 & 0 & \mu \end{pmatrix}$ is determined by two Lamé constants λ and μ, characterizing the elasticity of the cell. Values of λ and μ are listed in Supplementary Table 2.

As the strain tensor $\boldsymbol{\epsilon}(\boldsymbol{x})$ is related to the displacement vector $\boldsymbol{u}(\boldsymbol{x})$ through the relationship of

$\boldsymbol{\epsilon}(\boldsymbol{x}) = \boldsymbol{B}\boldsymbol{u}(\boldsymbol{x})$ [3], where $\boldsymbol{B} = \begin{pmatrix} \partial/\partial x_1 & 0 \\ 0 & \partial/\partial x_2 \\ \partial/\partial x_2 & \partial/\partial x_1 \end{pmatrix}$, , the overall free energy E_Ω of the cell Ω can be written as

$$\begin{aligned} E_\Omega = \frac{1}{2}\int_\Omega \boldsymbol{u}(\boldsymbol{x})^T \boldsymbol{B}^T \boldsymbol{D}\boldsymbol{B}\boldsymbol{u}(\boldsymbol{x})d\boldsymbol{x} - \int_\Omega (\sigma_a, \sigma_a, 0)\boldsymbol{\epsilon}(\boldsymbol{x})d\boldsymbol{x} + \frac{Y}{2}\int_\Omega \boldsymbol{u}(\boldsymbol{x})^2 d\boldsymbol{x} \\ + \sum_{\Omega \bigcap \Omega_n \neq \emptyset} \int_{\Omega \bigcap \Omega_n} f_a \boldsymbol{n}(\boldsymbol{x})^T \boldsymbol{u}(\boldsymbol{x})d\boldsymbol{x} - \int_\Omega \boldsymbol{f}(\boldsymbol{x})^T \boldsymbol{u}(\boldsymbol{x})d\boldsymbol{x}. \end{aligned} \tag{1}$$

The deformed cell under forces reaches its balance state when the strain energy of the cell E_Ω reaches minimum, at which we have $\partial E_\Omega(\boldsymbol{u})/\partial \boldsymbol{u} = 0$.

To calculate the displacement $\boldsymbol{u}(\boldsymbol{x})$ of a location $\boldsymbol{x} = (x_1, x_2)$ in a triangular element $\boldsymbol{\tau}_{i,j,k} \in T_\Omega$ from Eqn (1), we applied the stiffness matrix method to $\boldsymbol{\tau}_{i,j,k}$. The displacement vector $\boldsymbol{u}(\boldsymbol{x})$ can be interpolated from the displacement vectors of the three vertices $\boldsymbol{x}_i = (x_{i,1}, x_{i,2})$, $\boldsymbol{x}_j = (x_{j,1}, x_{j,2})$, and $\boldsymbol{x}_k = (x_{k,1}, x_{k,2})$ of $\boldsymbol{\tau}_{i,j,k}$ and the barycentric coordinates $\boldsymbol{\lambda} \equiv (\lambda_i(\boldsymbol{x}), \lambda_j(\boldsymbol{x}), \lambda_k(\boldsymbol{x}))$ of $\boldsymbol{x}$:

$$\boldsymbol{u}(\boldsymbol{x}) = \sum_{l \in \{i,j,k\}} \lambda_l(\boldsymbol{x}) \boldsymbol{u}_l(\boldsymbol{x}). \tag{2}$$

Here $\boldsymbol{\lambda}$ is determined by $\boldsymbol{\lambda} = \begin{pmatrix} 1 & 1 & 1 \\ x_{i,1} & x_{j,1} & x_{k,1} \\ x_{i,2} & x_{j,2} & x_{k,2} \end{pmatrix}^{-1} \begin{pmatrix} 1 \\ x_1 \\ x_2 \end{pmatrix}$, which can be rewritten as

$$\boldsymbol{\lambda} = \frac{1}{2|\boldsymbol{\tau}_{i,j,k}|} \begin{pmatrix} a_i & b_i & c_i \\ a_j & b_j & c_j \\ a_k & b_k & c_k \end{pmatrix} \begin{pmatrix} 1 \\ x_1 \\ x_2 \end{pmatrix}, \tag{3}$$

where $|\boldsymbol{\tau}_{i,j,k}|$ is the area of the triangle $\boldsymbol{\tau}_{i,j,k}$, $a_i = x_{j,1}x_{k,2} - x_{k,1}x_{j,2}$, $a_j = x_{i,1}x_{k,2} - x_{k,1}x_{i,2}$, $a_k = x_{i,1}x_{j,2} - x_{i,1}x_{j,2}$, $b_i = x_{j,2} - x_{k,2}$, $b_j = x_{k,2} - x_{i,2}$, $b_k = x_{i,2} - x_{j,2}$, $c_i = x_{j,1} - x_{k,1}$, $c_j = x_{k,1} - x_{i,1}$, and $c_k = x_{i,1} - x_{j,1}$.

From Eqn (2) and Eqn (3), $\frac{\partial \boldsymbol{u}(\boldsymbol{x})}{\partial x_1}$ can be written as

$$\frac{\partial \boldsymbol{u}(\boldsymbol{x})}{\partial x_1} = \frac{\partial \sum_{l \in \{i,j,k\}} \lambda_l u_l(\boldsymbol{x})}{\partial x_1} = \sum_{l \in \{i,j,k\}} \frac{b_l}{2|\tau_{i,j,k}|} u_l(\boldsymbol{x}).$$

Similarly $\frac{\partial \boldsymbol{u}(\boldsymbol{x})}{\partial x_2}$ can be written as

$$\frac{\partial \boldsymbol{u}(\boldsymbol{x})}{\partial x_2} = \sum_{l \in \{i,j,k\}} \frac{c_l}{2|\tau_{i,j,k}|} u_l(\boldsymbol{x}).$$

The strain-displacement matrix $\boldsymbol{B}_\tau$ for the displacement vector $\boldsymbol{u}_\tau = (\boldsymbol{u}_i, \boldsymbol{u}_j, \boldsymbol{u}_k)^T$ of $\boldsymbol{\tau}_{i,j,k}$, corresponding to the continuous version of $\boldsymbol{B} = \begin{pmatrix} \partial/\partial x_1 & 0 \\ 0 & \partial/\partial x_2 \\ \partial/\partial x_2 & \partial/\partial x_1 \end{pmatrix}$ of Eqn (1), takes the form of $\boldsymbol{B}_\tau = \frac{1}{2|\boldsymbol{\tau}_{i,j,k}|}\begin{pmatrix} b_i & 0 & b_j & 0 & b_k & 0 \\ 0 & c_i & 0 & c_j & 0 & c_k \\ c_i & b_i & c_j & b_j & c_k & b_k \end{pmatrix}$. In addition, $\int_\tau (\sigma_a, \sigma_a, 0)\boldsymbol{B}_\tau \boldsymbol{u}_\tau(\boldsymbol{x})d\boldsymbol{x} = \int_\tau \sigma_a \nabla \cdot \boldsymbol{u}_\tau(\boldsymbol{x})d\boldsymbol{x}$. According to Gauss's divergence theorem, $\int_\tau \sigma_a \nabla \cdot \boldsymbol{u}_\tau(\boldsymbol{x})d\boldsymbol{x} = \int_{\partial\tau} \sigma_a \boldsymbol{n}(\boldsymbol{x})^T \boldsymbol{u}_\tau(\boldsymbol{x})d\boldsymbol{x}$. The free energy E_τ of $\boldsymbol{\tau}_{i,j,k}$ can be rewritten following Eqn (1) as

$$\begin{aligned} E_\tau = \frac{1}{2}\int_\tau \boldsymbol{u}_\tau(\boldsymbol{x})^T \boldsymbol{B}_\tau^T \boldsymbol{D}\boldsymbol{B}_\tau \boldsymbol{u}_\tau(\boldsymbol{x})d\boldsymbol{x} - \int_{\partial\tau} \sigma_a \boldsymbol{n}(\boldsymbol{x})^T \boldsymbol{u}_\tau(\boldsymbol{x})d\boldsymbol{x} + \frac{Y}{2}\int_\tau \boldsymbol{u}_\tau(\boldsymbol{x})^2 d\boldsymbol{x} \\ + \sum_{\Omega \bigcap \Omega_n \neq \emptyset} \int_{\partial\tau \in \Omega \bigcap \Omega_n} f_a \boldsymbol{n}(\boldsymbol{x})^T \boldsymbol{u}_\tau(\boldsymbol{x})d\boldsymbol{x} - \int_\tau \boldsymbol{f}(\boldsymbol{x})^T \boldsymbol{u}_\tau(\boldsymbol{x})d\boldsymbol{x}, \end{aligned} \tag{4}$$

where $\boldsymbol{f}(\boldsymbol{x}) = (\lambda_i \boldsymbol{f}_i(\boldsymbol{x}), \lambda_j \boldsymbol{f}_j(\boldsymbol{x}), \lambda_k \boldsymbol{f}_k(\boldsymbol{x}))$, with $\boldsymbol{f}_i(\boldsymbol{x}), \boldsymbol{f}_j(\boldsymbol{x}), \boldsymbol{f}_k(\boldsymbol{x})$ the force vectors applied to the three vertices of $\boldsymbol{\tau}_{i,j,k}$.

We can find the solution to the problem of deformation under forces with the assumption that the free energy of $\boldsymbol{\tau}_{i,j,k}$ reaches its minimum at the stationary state, which happens when $\partial E_\tau / \partial \boldsymbol{u}_\tau(\boldsymbol{x}) = 0$. After taking the derivatives, we can rewrite the equilibrium equation for the element $\tau_{i,j,k}$ as

$$\begin{aligned} \int_\tau \boldsymbol{B}_\tau^T \boldsymbol{D}\boldsymbol{B}_\tau \boldsymbol{u}_\tau(\boldsymbol{x})d\boldsymbol{x} - \int_{\partial\tau \in \partial\Omega} \sigma_a \boldsymbol{n}(\boldsymbol{x})^T d\boldsymbol{x} + Y\int_\tau \boldsymbol{u}_\tau(\boldsymbol{x})d\boldsymbol{x} \\ + \sum_{\Omega \bigcap \Omega_n \neq \emptyset} \int_{\partial\tau \in \Omega \bigcap \Omega_n} f_a \boldsymbol{n}(\boldsymbol{x})^T d\boldsymbol{x} - \int_\tau \boldsymbol{f}(\boldsymbol{x})^T d\boldsymbol{x} = 0. \end{aligned} \tag{5}$$

Assuming the element $\boldsymbol{\tau}_{i,j,k}$ is of unit thickness t_τ, the element stiffness matrix $\boldsymbol{K}_\tau$ of $\tau_{i,j,k}$ is

$$\boldsymbol{K}_\tau \equiv \int_\tau \boldsymbol{B}_\tau^T \boldsymbol{D}\boldsymbol{B}_\tau d\boldsymbol{x} + Y\int_\tau d\boldsymbol{x} = t_\tau |\boldsymbol{\tau}_{i,j,k}| \boldsymbol{B}_\tau^T \boldsymbol{D}\boldsymbol{B}_\tau + Y|\boldsymbol{\tau}_{i,j,k}|\boldsymbol{I},$$

where $\boldsymbol{I}$ is identity matrix. The force $\boldsymbol{f}_\tau$ acting on $\boldsymbol{\tau}_{i,j,k}$ is

$$\begin{aligned} \boldsymbol{f}_\tau &\equiv \int_\tau \boldsymbol{f}(\boldsymbol{x})^T d\boldsymbol{x} + \int_{\partial\tau \in \partial\Omega} \sigma_a \boldsymbol{n}(\boldsymbol{x})^T d\boldsymbol{x} - \sum_{\Omega \bigcap \Omega_n \neq \emptyset} \int_{\partial\tau \in \Omega \bigcap \Omega_n} f_a \boldsymbol{n}(\boldsymbol{x})^T d\boldsymbol{x} \\ &= t_\tau \frac{|\boldsymbol{\tau}_{i,j,k}|}{3}(\boldsymbol{f}_i, \boldsymbol{f}_j, \boldsymbol{f}_k)^T + (e_i, e_j, e_k)^T \circ (\boldsymbol{n}_i, \boldsymbol{n}_j, \boldsymbol{n}_k)^T, \end{aligned} \tag{6}$$

where $e_l = \sigma_a |\partial\tau| \delta(l \in \partial\Omega) - f_a |\partial\tau| \delta(l \in \Omega \bigcap \Omega_n)$, $l = i, j, k$. From Eqn (5), we obtain the linear equation $\boldsymbol{K}_\tau \boldsymbol{u}_\tau = \boldsymbol{f}_\tau$ for element $\boldsymbol{\tau}_{i,j,k}$.

We can then gather the element stiffness matrices of all elements in all cells and assemble them into

one global stiffness matrix $\boldsymbol{K}$. The linear relationship between the concatenated vector $\boldsymbol{u}$ of all vertices in the mesh and the force vector $\boldsymbol{f}$ on all vertices is then given by:

$$\boldsymbol{K}\boldsymbol{u} = \boldsymbol{f}. \tag{7}$$

The behavior of the whole tissue in stationary state at a specific time step then can be obtained by solving this linear equation. For vertex $\boldsymbol{v}_i$ at $\boldsymbol{x}_i$, its new location is then updated as $\boldsymbol{x}_i' = \boldsymbol{x}_i + \boldsymbol{u}(\boldsymbol{v}_i)$.

Viscosity can be neglected in our model

Following previous studies [4,5], we assume that linear elasticity can adequately describe cell deformation under both external and internal forces during a time interval. Here we show that linear viscoelastic is unnecessary. A model of linear viscoelasticity can be expressed as a Prony series expansion of the stress relaxation as a function of time step Δt [6, 7]

$$E(\Delta t) = E_\infty + \sum_{j=1}^{N} E_j e^{-\frac{\Delta t}{\tau_j}},$$

where E_∞ is the long-term elastic modulus, E_j is the elastic coefficient of viscoelastic element j among the total N elements, $\tau_j = \eta_j / E_\infty$ is the relaxation time of the element j, η_j is the viscous coefficient of element j. The value of τ_j is usually 1 to 10 seconds [8]. In our model, the time step Δt is fixed as 30 minutes. Therefore, the term $\sum_{j=1}^{N} E_j e^{-\frac{\Delta t}{\tau_j}}$ can be treated as zero. Hence the effect of viscosity can be neglected. That is, the stress in our model in each time step of 30 minutes is only related to the long term elastic coefficient of the cell. We can therefore assume that linear elasticity is adequate in describing cell deformation in our model.

Supplementary Text 2

Cell-cell collision and its correction

It is important to detect collision when the bodies of two cells collide, to resolve the collision, and to restructure their contacting surfaces.

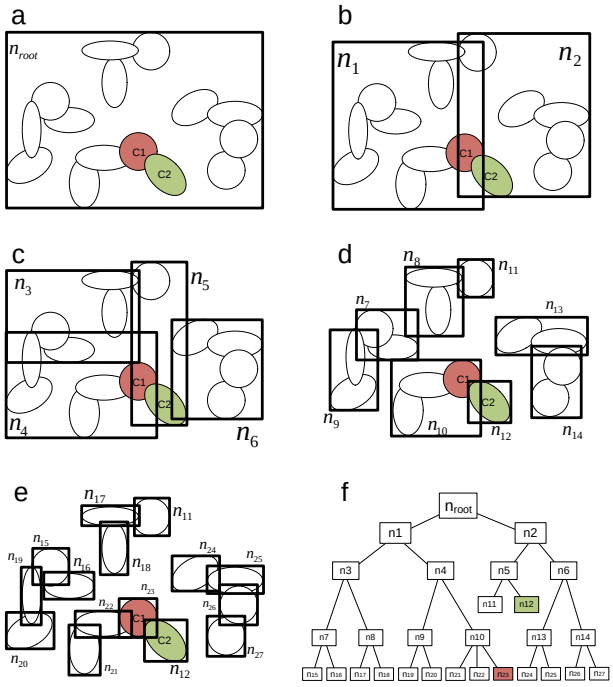

Figure 1. The Bounded Deformation (BD)-Tree structure for detecting collided cells. (a–e) The bounding boxes of at different levels of the BD-Tree. (e) Two potentially colliding cells $C1$ (red) and $C2$ (green) are detected by examining the intersection of their bounding boxes of n_{23} and n_{12}. (f) The BD-Tree from the root containing all cells to the leaf node level, where each node contains a single cell.

Cell collision detection

We use the technique of Bounded Deformation Tree (BD-Tree) to identify potential collision between a pair of cells [9]. Each node of the BD-Tree represents a bounding box that encloses a group of cells. The root node n_{root} contains all cells (Figure 1a) and has two daughter nodes n_1 and n_2, each containing roughly half of the cells grouped according to their distances to each other (Figure 1b). This division

process is then repeated recursively until we reach the leaf nodes, each of which containing only one cell (Figure 1c–1e).

For each cell, we use the bounding box it is contained in to identify potentially colliding cells. We start at the root of the BD-Tree and examine if box-intersection occurs at the next level. This is repeated until we have reached the leaf nodes and identified all potentially colliding cell-pairs (Figure 1f).

Resolving cell collision

Once a pair of potentially colliding cells Ω_1 and Ω_2 are identified, axis-aligned bounding boxes [10] are generated, and a 4-level quad-tree is constructed to represent each cell. The locations of edge intersections between the two cells are then identified by testing $(n_1 - 1) \times (n_2 - 1)$ pairs of edges, with n_1 and n_2 the number of vertices of Ω_1 and Ω_2 inside the aligned bounding boxes, respectively. There are two intersecting edge-pairs, with the fractions of the overlapping cell boundaries $\partial\Omega_1 \cap \partial\Omega_2$ between them (Fig 2a). Once the overlapping portions are identified, they are repaired using the *Cell-merge* primitive described below, which generates a new contacting surface between previously colliding cells. This initial contacting surface is then subject to relaxation from the elasticity of Ω_1 and Ω_2 in the next time step.

Primitives for topologic and geometric changes

There are five Primitives we use to model topologic and geometric changes during cell growth, proliferation, and migration. These Primitives are:

- P1. *Cell-merge*: When two cells in collision are identified, the spatial locations of vertices in each cell in the intersecting surfaces are updated so the overlaps between cells are repaired. The new contacting surfaces from the two cells are defined by a set of vertices where both surfaces are attached. The attached vertices from the two cells are paired with attachment of adhesion linkages sharing the same coordinates (Fig 2a).

- P2. *Cell-separation*: When a pair of attached vertices with an adhesion linkage on the contacting surfaces of two cells experience contraction force larger than the threshold f_θ, we remove the kinematic attachment of the adhesion linkage between them and these two vertices become separated (Fig 2b).

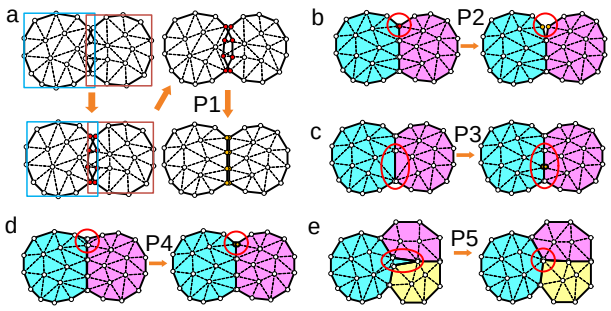

Figure 2. Primitives for cell geometric and topologic changes. (a) P1. *Cell-merge*: The overlapping surfaces of the two colliding cells are detected by examining the intersection of their bounding boxes. The overlapping surfaces (the red vertices in the intersection of bounding boxes) are then replaced by the contacting surfaces composed by the attached vertices with adhesion linkages. (b) P2. *Cell-separation*: Previously attached vertices on the contacting surfaces of two different cells are separated from each other. (c) P3. *Edge-subdivision*: When an edge becomes longer than a predefined threshold of $2|\boldsymbol{e}_\theta|$, it is subdivided by adding a new vertex at the midpoint. (d) P4. *Edge-simplification*: when an edge becomes shorter than a predefined threshold of $|\boldsymbol{e}_\theta|/2$, we remove the starting vertex of this edge (counter clock-wise), as well as the preceding edge and the succeeding edge of that vertex. We then directly connect its preceding and the succeeding vertices with a new edge. (e) P5. *Sliver-removal*: When a skinny triangle with an angle smaller than a predefined threshold $\theta_S = 19^\circ$ [11] appears, we remove this skinny triangle, two of its edges, and one of its vertices. A new edge is then added to connect the two remaining vertices.

- P3. *Edge-subdivision*: When an edge becomes longer than a predefined threshold of $2|\boldsymbol{e}_\theta|$, we subdivide this edge by adding a new vertex at its midpoint (Fig 2c).

- P4. *Edge-simplification*: When an edge becomes shorter than a predefined threshold of $|\boldsymbol{e}_\theta|/2$, we remove the starting vertex of this edge (counter clock-wise), as well as the preceding edge and the succeeding edge of that vertex. We then directly connect its preceding and the succeeding vertices with a new edge (Fig 2d).

- P5. *Sliver-removal*: When a skinny triangle with an angle smaller than a predefined threshold $\theta_S = 19°$ [11] appears, the high aspect ratio of its longest edge and its shortest edge causes numerical instability in finite element calculation [11]. We therefore remove this skinny triangle, two of its edges, and one of its vertices. A new edge is then added to connect the two remaining vertices (Fig 2e).

All topological changes can be realized

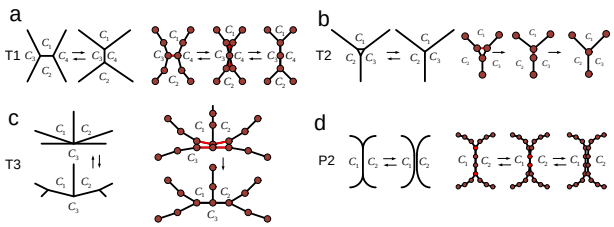

Figure 3. Combination of primitives in this study can realize all cell topologic changes in vertex cell model as well as the introduction of a new type of topologic change. (a) The Recombination move (T1, left) is realized by one *edge-simplification* primitive on the edge connecting C_1 and C_2, followed by two *sliver-removal* primitives for C_1 and C_2 each. (b) The Disappearance move (T2, left) is realized by three *edge-simplification* primitives for C_1, C_2, and C_3 each. (c) The Adhesion move (T3, left) is realized by two *cell-merge* primitives for the C_1-C_3 pair and the C_2-C_3 pair. (d) We introduce a new type of topological change called *Cell-separation* (P2, left), namely, the separation of a pair of contacting cells in our model. One *cell-separation* primitive between neighboring cells C_1 and C_2 is shown.

In the vertex cell model, three elementary moves can exhaust all possible topological changes except cell pair separation. These moves are called Recombination (T1), Disappearance (T2), and Adhesion (T3) [12]. These three moves can be realized using Primitives P1–P5 described in this study (Figure 3a–3c; Supplementary Video 4 shows the T1 process realized using our model). In addition to topological changes of T1–T3, we introduced one new topological change, called *Cell-separation* (P2), which separates

a pair of contacting cells (Figure 3d).

Supplementary Text 3

Diffusion of growth factor

In our model, diffusion of each growth factor in the tissue is modeled with the assumption that cells are compartments with well-mixed growth factors. We have the following diffusion equation:

$$\frac{d\boldsymbol{x}(s,t)}{dt} = \boldsymbol{D}\Delta\boldsymbol{x}_k(s,t), \tag{8}$$

where s is the spatial coordinates, $\boldsymbol{x}(s,t)$ is the concentration vector of different growth factors at s, and $\boldsymbol{D}$ is the vector of diffusion coefficients of growth factors.

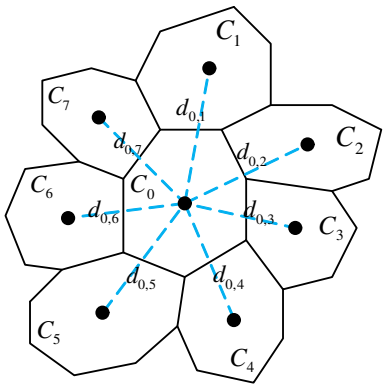

Figure 4. Diffusion of growth factors in tissue. Diffusion of each growth factor in tissue is modeled using cells as homogeneous elements. The distance $d_{i,j}$ between centers of two neighboring cells are taken as the diffusion distances.

We then discretize Eqn (8) by cell elements as shown in Figure 4:

$$\frac{d\boldsymbol{x}(i,t)}{dt} = \boldsymbol{D}\sum_{j,\,C_i\bigcap C_j\neq\emptyset}\frac{\boldsymbol{x}(j,t)-\boldsymbol{x}(i,t)}{d_{i,j}^2}, \tag{9}$$

where $\boldsymbol{x}(i,t)$ is the state vector of growth factor concentrations in cell i at time t, $d_{i,j}$ is the center-to-center distance between cell i and a neighboring cell j. Eqn (9) can be expressed equivalently for growth factor k in cell i as:

$$\frac{dx_k(i,t)}{dt} = \sum_{j,C_i\bigcap C_j\neq\emptyset}A_{k,i,j}x_k(j,t), \tag{10}$$

where $A_{k,i,j} = \frac{D_k}{d_{i,j}^2}$ for all $i \neq j$, and $A_{k,i,j} = -\sum_{i,\,C_i\bigcap C_j\neq\emptyset}\frac{D_k}{d_{i,j}^2}$ for $i = j$, with D_k being the diffusion

coefficient of growth factor k. This can be re-written in the matrix form as

$$\frac{d\boldsymbol{x}_k(t)}{dt} = \boldsymbol{A}_k \boldsymbol{x}_k(t), \tag{11}$$

where $\boldsymbol{x}_k(t)$ is the concatenated vector of $x_k(i,t)$ for each cell i, $\boldsymbol{A}_k$ is the matrix whose element is $A_{k,j,i}$. The vector of growth factor concentration in each cell i, namely, $\boldsymbol{x}(i,t)$ is then updated by solving Eqn (11).

The contour plots of computed EGF concentration from solving Eqn (11) in the wound tissue at different time steps under chemotaxis and cohesotaxis are shown as an example in Figure 5. EGF is synthesized in the wound bed area and diffuse to the areas around the wound bed. As the wound bed is covered by the migrating keratinocytes, EGF concentration decreases and eventually disappears when the wound bed is completely repaired.

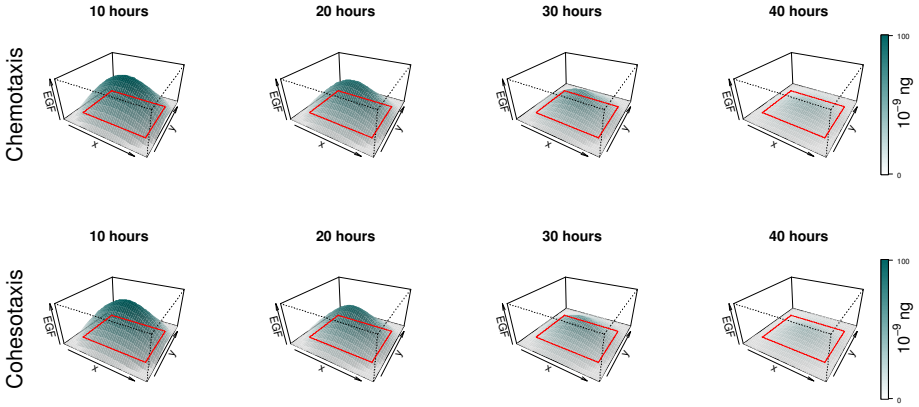

Figure 5. Contour plots of EGF concentration in the tissue at different time steps under chemotaxis and cohesotaxis. The red boxes indicate the wound edge at initiate time.

Supplementary Text 4

Cell behaviors during re-epithelialization

Control of cell growth and proliferation. A cell grows and then divides into two daughter cells during one cell cycle [13]. The duration of the cell cycle is cell-type specific, but is also influenced by growth factors such as KGF and EGF [14, 15]. We follow ref [16] and regard cell growth as a process driven by the increased pressure resulting from the accumulation of soluble material inside the cell body. In our model, we assume that the incremental changes in cell volume is according to the elasticity of the cell. The growth rate r_Ω of a cell Ω, namely, its volume increment per unit time, is then modeled as:

$$r_\Omega = \frac{|\Omega|(1 + k_{\mathrm{KGF}} \log(y_{\mathrm{KGF}}))(1 + k_{\mathrm{EGF}} \log(y_{EGF}))}{\Delta T_\Omega}, \tag{12}$$

where $|\Omega|$ is the volume of the cell before growth, ΔT_Ω the time duration of a full cell cycle of cell Ω, k_{KGF} and k_{EGF} are coefficients, y_{KGF} and y_{EGF} are the concentrations of KGF and EGF, respectively. For cell Ω growing from time t to $t + \Delta t$, the incremental volume $\Delta|\Omega|$ is calculated as $\Delta|\Omega| = r_\Omega \Delta t$. When the area of Ω is doubled, we divide the cell Ω into two daughter cells by adding a set of paired vertices along the shortest axis of Ω.

Force model of cell migration. Here the magnitude of the protrusion force per unit length on the leading edges is modeled as $f_{af} = 6nN/\mu M$, following the elastic ratchet model [17,18] (see Supplementary Table 2 for parameter values associated with f_{af}).

Cell apoptosis and wound element removal. During the re-epithelialization process, keratinocytes migrate into the wound bed and clear up the fibrin clot [19]. To model the degradation of wound element by a keratinocyte, we remove the site of wound element when a migrating keratinocyte overlaps with it. In addition, if a keratinocyte in the tissue apoptosizes, it is also removed from the system. Details are described in ref [20].

Supplementary Text 5

The model of purse string mechanism

Cell crawling and acto-myosin cable contraction in a purse-string manner are the two well-known mechanisms driving epithelial wound closure [21]. While the purse-string mechanism plays dominant roles in the closure of small defects during wound healing [22, 23], where the wound size is that of about 20 cells [24, 25], our study focus on closure of wounds with larger size where the cell crawling mechanism driven by protrusion takes the dominant role [26]. Therefore, we do not consider the purse-string mechanism in the current model.

Our preliminary exploration showed that the purse-string mechanism can be incorporated to study the closure of a small wound (e.g., an *in silico* size of 90 $\mu m\times$ 90 μm, Fig 6a) once a curvature $\kappa(\boldsymbol{x})$-dependent purse-string tension force term $\boldsymbol{T}(\boldsymbol{x})$ is added. As shown in Figure 6b, the wound shape under purse string mechanism is more regular, while the wound shape without string tension is irregular, with some islands of smaller wound gaps (Figure 6c).

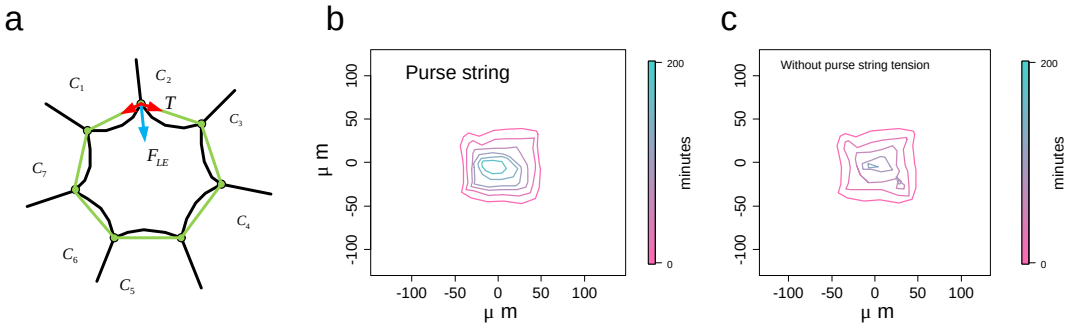

Figure 6. The purse string mechanism for wound closure and the contours of wound boundaries over time. (a) The purse string along the wound boundary cells can be modeled as line segments (green) connecting vertices on the wound boundary between cells. The string tension T is along the direction of purse string (red). The epidermis force F_{LE} is along the normal of the purse string (blue). (b) contour of wound boundaries under purse string mechanism. (c) the contour of wound boundaries when there is no string tension.

Supplementary Text 6

Temporal pattern of wound closure ratio

Previous studies show that the re-epithelialization rate is around 300 $\mu m/d$ [27, 28]. According to this rate, it would take about 1 to 2 days to achieve complete wound closure for a wound bed with a size of 800 μm × 300 μm as we used in this study. Here we compare the wound closure ratio, $\rho(t_n)$ under chemotaxis and cohesotaxis with previous wound healing study by Safferling, et al [28]. In their study, it took 4 days to achieve complete wound closure $\rho(t_n) = 1$ [28]. In our study, it took 52 and 57 hours to achieve complete wound closure for cohesotaxis and chemotaxis, respectively. The half diagonal length of the wound we used is $\sqrt{400^2 + 150^2}\mu m$. Then the ratio of wound radius of the study by Safferling, et al [28] over our study is $\frac{1000\mu m}{\sqrt{400^2+150^2}\mu m} = 2.3$. The ratio of wound closure time of their study over our study is $\frac{96h}{48h} = 2$. Since these two ratios have similar scale, we can compare the curves of the wound closure rate of our results with that from Safferling, et al [28]. We mapped the timeline from Safferling, et al [28] to our timeline by mapping 1 day to 12 hours. We found that the temporal pattern of wound closure ratio along with the timeline under both chemotaxis and cohesotaxis are similarly matched with the experimental data (Fig 7). This suggested that the temporal pattern of wound closure of our simulation is generally consistent with the experimental study.

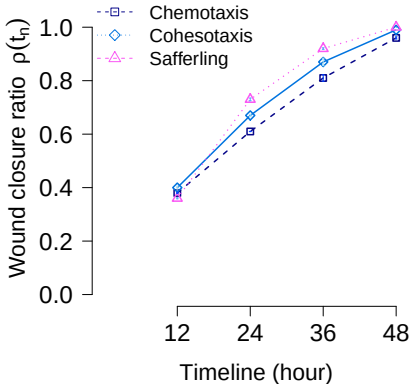

Figure 7. Wound closure ratio under chemotaxis and cohesotaxis comparing to previous experimental study [28]. Wound closure ratio at 12, 24, 36, 48 hour under chemotaxis and cohesotaxis and the wound closure ratio at 1 day (map to 12 hour), 2 day (map to 24 hour), 3 day (map to 36 hour), 4 day (map to 48 hour) by Safferling, et al [28] are shown respectively.

Supplementary Text 7

Sensitivity of the results with different size of time step

In our model, the time step size is fixed to 30 minutes for ease of modeling as the cytoskeleton remodeling time of a cell is also about 30 minutes [29]. We examine how the size of time step would influence our simulation results. We chose two additional time step size of 60 minutes and 20 minutes. As the time step size decreased from 60 minutes to 30 minutes and further to 20 minutes, the wound closure time increased from 53±1 hours (60 minutes) to 57±1 hours (30 minutes), and then slightly to 58±1 hours (20 minutes) under chemotaxis. Under cohesotaxis, the wound closure time increased from 48±1 hours (60 minutes) to 52±1 hours (30 minutes), and then slightly to 53±1 hours (20 minutes) (Figure 8a and 8b). Under chemotaxis the fraction of direction angle $\alpha(t_n) \leq 30^\circ$ decreased from 45±1% (60 minutes) to 40±2% (30 minutes), and remained as 40±1% (20 minutes). Under cohesotaxis, this measurement decreased from 32±2% (60 minutes) to 28±1% (30 minutes), and remained as 28±1% (20 minutes) (Figure 8c and 8d). Under chemotaxis, the migration persistence ratio $p(t_n)$ decreased from 86±1% (60 minutes) to 79±1% (30 minutes), and remained as 79±1% (20 minutes) in Region I while it decreased from 80±1% (60 minutes) to 73±1% (30 minutes), and remained as 73±1% (20 minutes) in Region II (Figure 8e). Under cohesotaxis, this measurement decreased from 79±2% (60 minutes) to 73±2% (30 minutes), and remained as 73±1% (20 minutes) in Region I, and decreased from 73±2% (60 minutes) to 66±1% (30 minutes), and decreased slightly to 65±2% (20 minutes) in Region II (Figure 8e). Under chemotaxis, the normalized separation distance $d_{i,j}(t_n)$ increased slightly from 0.13±0.01 (60 minutes) to 0.14±0.01 (30 minutes), and then decreased to 0.13±0.01 (20 minutes) in Region I while it decreased from 0.24±0.01 (60 minutes) to 0.22±0.01 (30 minutes), and to 0.21±0.01 (20 minutes) in Region II (Figure 8f). Under cohesotaxis, this measurement decreased from 0.17±0.01 (60 minutes) to 0.15±0.01 (30 minutes), and to 0.14±0.01 (20 minutes) in Region I while it decreased from 0.16±0.01 (60 minutes) to 0.14±0.01 (30 minutes), and to 0.13±0.01 (20 minutes) in Region II (Figure 8f).

As shown in Figure 8, overall, there are small differences between results obtained using time step of 30 minutes and using time step of 60 minutes, while the results using 30 minutes and 20 minutes are practically the same. Computed results converge as the step size is decreased from 30 minutes to 20 minutes. For example, the temporal pattern of wound closure ratio and spatial pattern of direction angle under 30 minutes and 20 minutes are almost the same. In addition, the overall pattern of chemotaxis and

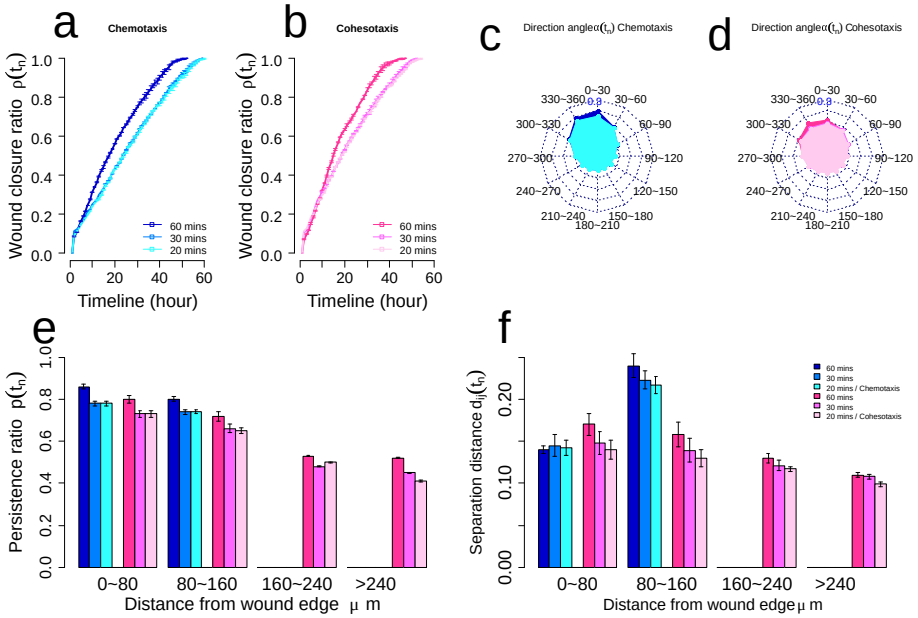

Figure 8. Effects of time step size on simulation results. (a-f) The wound closure ratio $\rho(t_n)$ (a-b), the direction angle $\alpha(t_n)$ (c-d), persistence ratio $p(t_n)$ (e), and the normalized separation distance $d_{i,j}(t_n)$ (f) under chemotaxis and cohesotaxis using different time step size: 60 minutes, 30 minutes and 20 minutes, respectively. The error bars depict the standard deviation of three simulation runs.

cohesotaxis are not affected by different choice of time steps of 60 minutes, 30 minutes, and 20 minutes. In each case, we observe that cell migration achieves more accurate directionality and higher persistence under regulation of biochemical cue. Collective cell migration are better coordinated under regulation of mechanical cue. Therefore, the choice of the time step size of 30 minutes used in this study is well justified.

Supplementary Text 8

Re-epithelialization under non-proliferative conditions

Cell proliferation plays important roles in providing fresh new cells for wound repair. However, some previous studies showed that wounded tissue with small wound can close the wound without the cell proliferation [22, 23, 26]. Here we studied the tissue patterns of re-epithelialization process under non-proliferative conditions. To inactivate the cell proliferation in our *in silico* simulation, we changed the scaling factor of cell proliferation score α_1 to zero, then no cells will take the behavior of proliferation during re-epithelialization.

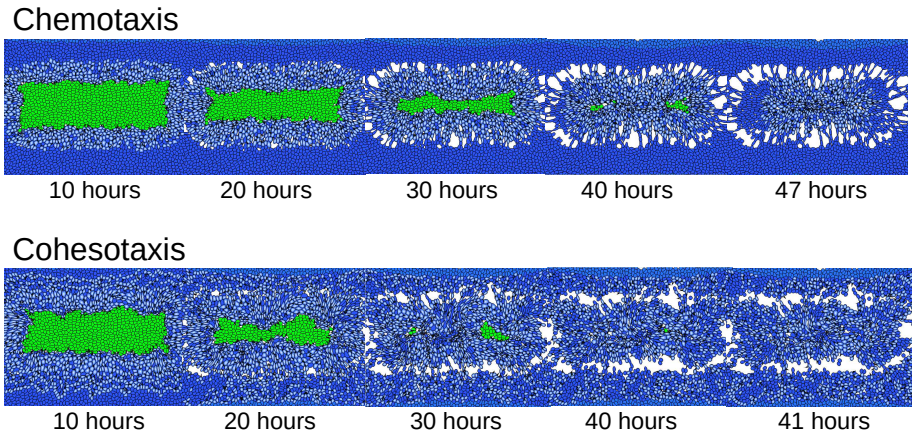

Figure 9. The snapshot of wound tissue under non-proliferative conditions. The re-epithelialization process under chemotaxis and cohesotaxis without cell proliferation. Blue: keratinocytes; Green: wound elements; Light blue: migrating keratinocytes. Re-epithelialization is faster under both chemotaxis and cohesotaxis under non-proliferating condition: 47 vs. 57 hours under chemotaxis and 41 hours vs. 52 hours under cohesotaxis. In addition, there are large lesion and unsealed gaps remaining.

Our results showed that for both chemotaxis and cohesotaxis under non-proliferative condition, it takes shorter time to close the wound than that under normal proliferative condition (47 hours versus 57 hours under chemotaxis and 41 hours versus 52 hours under cohesotaxis). This is due to the fact that since proliferation is inhibited, there are more cells migrating towards the wound bed, which expedite the wound closure process. However, there are large lesioned, unsealed gaps left in the tissue after the complete re-epithelialization under both chemotaxis and cohesotaxis (Figure 9) due to insufficient new

fresh cells generated to fill the wounded tissue. Our *silico* simulation suggests that cell proliferation is required for wounded tissue with large wound size.

Supplementary Figure 1

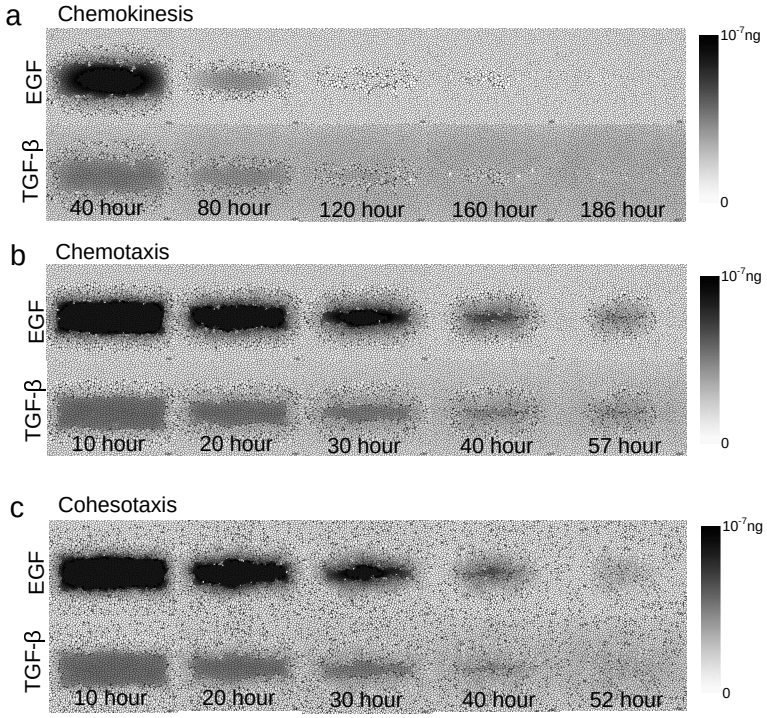

Figure S1. Concentration of growth factors at different time under three different guidance mechanisms of cell migration. (a) The concentrations of EGF and TGF-β under chemokinesis. (b) The concentrations of EGF and TGF-β under chemotaxis. (c) The concentrations of EGF and TGF-β under cohesotaxis.

Supplementary Table 1

Cell paracrine signaling network

Table S1. Relationships between cells and growth factors in our model. Details of each branch of the schematic diagram of the intracellular signaling network in our model are given, including the relevant references.

Species	Acts on	Activity	Branch number	Ref.
wound	KGF	Synthesis	1	[30]
	EGF	Synthesis	2	[31]
	TGF-β	Synthesis	3	[32]
keratinocyte	TGF-β	Synthesis	4	[32]
KGF	keratinocyte	Promotes proliferation	5	[32,33]
EGF	keratinocyte	Promotes proliferation and migration	6	[32,33]
TGF-β	keratinocyte	Inhibits proliferation	7	[32]

Supplementary Table 2

Model parameters

Table S2. Geometric, mechanical, chemical, and biological parameters used in our model. The first three parameters defined the geometry and time step of our model.

Name	description	value	Ref.
Model setup			
Δt	time step lapse	30 $minutes$	N/A
t_τ	thickness of cell	1 μm	N/A
$\|e_\theta\|$	edge length threshold	3.14 μm	N/A
r_Ω	radius of normal keratinocyte	$\sim$ 10 μm	[34]
θ_S	sliver-removal threshold	19°	[11]
Material properties (1)			
E_K	Young's modulus of keratinocyte	120 kPa	[35]
E_W	Young's modulus of wound type	400 kPa	[36]
ν	Poisson ratio	0.40	[37]
Y	Friction energy constant	0.9 $nN/\mu m^3$	[38]
σ_a	contractile pressure	2 kPa	[38]
Cell proliferation			
ΔT_Ω	human cell cycle time	24 $hours$	[39]
Cell migration and adhesion (2) (3)			
f_θ	rupture force of E-cadherin cell contacts	4.1 $nN/\mu m$	[40]
f_{af}	protrusion force	$\sim$ 6 $nN/\mu m$	[17, 18, 41]
f_a	cell-cell boundary adhesion force constant	2 $nN/\mu m$	[42]
Inter-cellular paracrine signaling			
D_{KGF}	diffusion rate of KGF	$4.9\times10^{-9} cm^2/s$	[43]
D_{EGF}	diffusion rate of EGF	$5.2\times10^{-9} cm^2/s$	[44]
$D_{TGF-\beta}$	diffusion rate of TGF-β	$2.9\times10^{-9} cm^2/s$	[45]
$\lambda_{s,KGF}$	synthesis rate of KGF	$0.40\times10^{-7} ng/cell/day$	[46]
$\lambda_{s,EGF}$	synthesis rate of EGF	$0.51\times10^{-6} ng/cell/day$	[47]
$\lambda_{s,TGF-\beta}$	synthesis rate of TGF-β	$0.13\times10^{-6} ng/cell/day$	[48]
$\lambda_{d,KGF}$	degradation rate of KGF	$1.1\times10^{-4}/min$	[49]
$\lambda_{d,EGF}$	degradation rate of EGF	$6.1\times10^{-4}/min$	[50]
$\lambda_{d,TGF-\beta}$	degradation rate of TGF-β	$2.5\times10^{-4}/min$	[51]

(1) Lam$\acute{e}$ constants λ and μ of keratinocytes and wound elements are calculated from the Young's modulus E and the Poisson ratio ν: $\lambda = E\nu/(1+\nu)(1-2\nu)$, $\mu = E/2(1+\nu)$. Poisson ratio ν measures the fractions of deformation of the material in directions orthogonal to that of the applied force. In our model, the Poisson ratio of the cell and wound element is fixed to 0.40 following previous computational

study [37]. (2) In our model, there is a prefixed cell thickness $t_\tau = 1\ \mu m$. Parameters associated with cell surface area in 3D are then converted by multiplying the value of cell thickness so they are associated with cell boundary lengths in 2D. For example, the rupture stress of cell-cell adhesion is now 4.1 $nN/\mu m$ instead of 4.1 $nN/\mu m^2$. (3) To estimate the value of protrusion force driving cell migration in one time step (30 minutes in our model), we take account the time length of maturation of focal complex. During cell migration, cell forms new focal complex on the leading edge upon increase in the concentration of actin filaments to generate protrusion force [52]. Since the maturation time of focal complex formation on the leading edge is approximately 60 seconds [41], we assume that the protrusion force is only activated after every 60 seconds. Therefore, there are approximately 30 rounds of activated protrusion force per unit length during one time step of 30 minutes. We then sum them over the one hour period to obtain the accumulated protrusion force $|f_{af}| = 6\ nN/\mu m$ per unit length within one time step. Each actin filament on the leading edge generates a protrusion force of $\sim$2 pN [17] and there are about 100 active filament per 1 μm on the leading edge [18].

Supplementary Table 3

Model parameters

Table S3. Parameters used to control cell behaviors in our model. The unit of cytokine concentration is $1 = 10^{-9}ng$. Any concentration less than $10^{-9}ng$ is rounded down to 0 to ensure the logarithm term is positive. Since cell migration is a key event for re-epithelialization, the scaling factor α_2 for cell migration is to have the same value as α_1 for cell proliferation such that the behavior of migration occurs as frequently as the behavior of proliferation in our model. We assigned very small value for α_3 for cell apoptosis as behavior of apoptosis rarely occurs for keratinocyte during re-epithelialization [53].

Name	description	value	Ref.
Stochastic control of cell behaviors			
α_1	scaling factor of stochastic control of cell proliferation	0.11	[54]
α_2	scaling factor of stochastic control of cell migration	0.11	Estimated
α_3	scaling factor of stochastic control of cell apoptosis	0.1×10^{-8}	Estimated
α_4	scaling factor of stochastic control of cell quiescence	0.78	Estimated
β^1_{KGF}	scaling factor of KGF promoting keratinocyte proliferation	0.0015	[54]
β^1_{EGF}	scaling factor of EGF promoting keratinocyte proliferation	0.035	[54]
$\beta^1_{TGF-\beta}$	scaling factor of TGF-β inhibiting keratinocyte proliferation	0.075	[55]
β^2_{EGF}	scaling factor of EGF promoting keratinocyte migration	0.05	[54]
Cell proliferation			
k_{EGF}	scaling factor of EGF decreasing cell cycle time	0.54	[56, 57]
k_{KGF}	scaling factor of KGF decreasing cell cycle time	0.14	[58, 59]

References

1. Moenning C, Dodgson NA (2003) Fast marching farthest point sampling for implicit surfaces and point clouds. Computer Laboratory Technical Report 565.

2. Edelsbrunner H (2001) Geometry and Topology for Mesh Generation. Cambridge Monographs on Applied and Computational Mathematics. Cambridge University Press.

3. Feng K, Shi Z (2013) Mathematical Theory of Elastic Structures. Springer Berlin Heidelberg.

4. Safran S, Gov N, Nicolas A, Schwarz U (2005) Physics of cell elasticity, shape and adhesion. Physica A: Statistical Mechanics and its Applications 352: 171–201.

5. Wei C, Lintilhac P, Tanguay J (2001) An insight into cell elasticity and load-bearing ability. measurement and theory. Plant Physiology 126: 1129–1138.

6. Bower A (2009) Applied Mechanics of Solids. CRC Press.

7. Sedef M, Samur E, Basdogan C (2006) Real-time finite-element simulation of linear viscoelastic tissue behavior based on experimental data. Computer Graphics and Applications, IEEE 26: 58–68.

8. Wottawah F, Schinkinger S, Lincoln B, Ananthakrishnan R, Romeyke M, et al. (2005) Optical rheology of biological cells. Physical review letters 94: 098103.

9. James DL, Pai DK (2004) Bd-tree: output-sensitive collision detection for reduced deformable models. ACM Transactions on Graphics (TOG) 23: 393–398.

10. Sulaiman HA, Othman M, Ismail M, Said M, Alice M, et al. (2013) Distance computation using axis aligned bounding box (aabb) parallel distribution of dynamic origin point. International Conference on Microelectronics 2013: 1–6.

11. Bern M, Eppstein D, Gilbert J (1994) Provably good mesh generation. Journal of Computer and System Sciences 48: 384–409.

12. Nagai T, Honda H (2009) Computer simulation of wound closure in epithelial tissues: Cell–basal-lamina adhesion. Physical Review E 80: 061903.

13. Alberts B (2008) Molecular Biology of the Cell. Garland Science.

14. Southgate J, Hutton K, Thomas D, Trejdosiewicz LK (1994) Normal human urothelial cells in vitro: proliferation and induction of stratification. Laboratory investigation: a Journal of Technical Methods and Pathology 71: 583–594.

15. Michelson PH, Tigue M, Panos RJ, Sporn PH (1999) Keratinocyte growth factor stimulates bronchial epithelial cell proliferation in vitro and in vivo. American Journal of Physiology-Lung Cellular and Molecular Physiology 277: L737–L742.

16. Ateshian GA, Morrison B, Holmes JW, Hung CT (2012) Mechanics of cell growth. Mechanics Research Communications 42: 118–125.

17. Mogilner A, Oster G (1996) Cell motility driven by actin polymerization. Biophysical Journal 71: 3030–3045.

18. Prass M, Jacobson K, Mogilner A, Radmacher M (2006) Direct measurement of the lamellipodial protrusive force in a migrating cell. The Journal of Cell Biology 174: 767–772.

19. Salo T, Mäkelä M, Kylmäniemi M, Autio-Harmainen H, Larjava H (1994) Expression of matrix metalloproteinase-2 and-9 during early human wound healing. J Technical Methods and Pathology 70: 176–182.

20. Kachalo S, Naveed H, Cao Y, Zhao J, Liang J (2015) Mechanical model of geometric cell and topological algorithm for cell dynamics from single-cell to formation of monolayered tissues with pattern. PloS ONE 10: e0126484.

21. Begnaud S, Chen T, Delacour D, Mege RM, Ladoux B (2016) Mechanics of epithelial tissues during gap closure. Current Opinion in Cell Biology 42: 52–62.

22. Rosenblatt J, Raff MC, Cramer LP (2001) An epithelial cell destined for apoptosis signals its neighbors to extrude it by an actin-and myosin-dependent mechanism. Current biology 11: 1847–1857.

23. Tamada M, Perez TD, Nelson WJ, Sheetz MP (2007) Two distinct modes of myosin assembly and dynamics during epithelial wound closure. The Journal of cell biology 176: 27–33.

24. Nier V, Deforet M, Duclos G, Yevick HG, Cochet-Escartin O, et al. (2015) Tissue fusion over nonadhering surfaces. Proceedings of the National Academy of Sciences 112: 9546–9551.

25. Vedula SRK, Peyret G, Cheddadi I, Chen T, Brugués A, et al. (2015) Mechanics of epithelial closure over non-adherent environments. Nature communications 6.

26. Ravasio A, Cheddadi I, Chen T, Pereira T, Ong HT, et al. (2015) Gap geometry dictates epithelial closure efficiency. Nature communications 6.

27. Laplante AF, Germain L, Auger FA, Moulin V (2001) Mechanisms of wound reepithelialization: hints from a tissue-engineered reconstructed skin to long-standing questions. The FASEB Journal 15: 2377–2389.

28. Safferling K, Sütterlin T, Westphal K, Ernst C, Breuhahn K, et al. (2013) Wound healing revised: A novel reepithelialization mechanism revealed by in vitro and in silico models. The Journal of Cell Biology 203: 691–709.

29. Osborn EA, Rabodzey A, Dewey CF, Hartwig JH (2006) Endothelial actin cytoskeleton remodeling during mechanostimulation with fluid shear stress. American Journal of Physiology-Cell Physiology 290: C444–C452.

30. Varani J, Perone P, Deming MO, Warner RL, Aslam MN, et al. (2009) Impaired keratinocyte function on matrix metalloproteinase-1 (mmp-1) damaged collagen. Arch Dermatological Res 301: 497–506.

31. Nickoloff B, Mitra R, Riser B, Dixit V, Varani J (1988) Modulation of keratinocyte motility. correlation with production of extracellular matrix molecules in response to growth promoting and antiproliferative factors. Am J Pathol 132: 543–551.

32. Larjava H, Häkkinen L, Koivisto L (2011) Re-epithelialization of wounds. Endodontic Topics 24: 59–93.

33. Santoro MM, Gaudino G (2005) Cellular and molecular facets of keratinocyte reepithelization during wound healing. Experimental Cell Research 304: 274–286.

34. Watt FM, Green H (1981) Involucrin synthesis is correlated with cell size in human epidermal cultures. The Journal of Cell Biology 90: 738–742.

35. Lulevich V, Yang Hy, Rivkah Isseroff R, Liu Gy (2010) Single cell mechanics of keratinocyte cells. Ultramicroscopy 110: 1435–1442.

36. Collet JP, Shuman H, Ledger RE, Lee S, Weisel JW (2005) The elasticity of an individual fibrin fiber in a clot. Proceedings of the National Academy of Sciences 102: 9133–9137.

37. Zielinski R, Mihai C, Kniss D, Ghadiali SN (2013) Finite element analysis of traction force microscopy: Influence of cell mechanics, adhesion, and morphology. Journal of Biomechanical Engineering 135: 071009.

38. Oakes P, Banerje S, Marchetti M, Gardel M (2014) Geometry regulates traction stresses in adherent cells. Biophysical Journal 107: 825–833.

39. Cooper G, Hausman R (2004) The Cell: A Molecular Approach. ASM Press.

40. Chu YS, Thomas WA, Eder O, Pincet F, Perez E, et al. (2004) Force measurements in e-cadherin–mediated cell doublets reveal rapid adhesion strengthened by actin cytoskeleton remodeling through rac and cdc42. The Journal of Cell Biology 167: 1183–1194.

41. Tozluoğlu M, Tournier AL, Jenkins RP, Hooper S, Bates PA, et al. (2013) Matrix geometry determines optimal cancer cell migration strategy and modulates response to interventions. Nature Cell Biology 15: 751–762.

42. Dong S, Long Z, Tang L, Jiang Y, Yan Y (2014) Simulation of growth and division of 3d cells based on finite element method. International Journal of Applied Mechanics 6: 1450041.

43. Bader RA, Herzog KT, Kao WJ (2009) A study of diffusion in poly (ethyleneglycol)-gelatin based semi-interpenetrating networks for use in wound healing. Polymer Bulletin 62: 381–389.

44. Thorne RG, Hrabětová S, Nicholson C (2004) Diffusion of epidermal growth factor in rat brain extracellular space measured by integrative optical imaging. Journal of Neurophysiology 92: 3471–3481.

45. Murphy KE, Hall CL, Maini PK, McCue SW, McElwain DS (2012) A fibrocontractive mechanochemical model of dermal wound closure incorporating realistic growth factor kinetics. Bulletin of Mathematical Biology 74: 1143–1170.

46. GRØN B, Stoltze K, Andersson A, Dabelsteen E (2002) Oral fibroblasts produce more hgf and kgf than skin fibroblasts in response to co-culture with keratinocytes. Apmis 110: 892–898.

47. Kurobe M, Furukawa S, Hayashi K (1985) Synthesis and secretion of an epidermal growth factor (egf) by human fibroblast cells in culture. Biochemical and Biophysical Research Communications 131: 1080–1085.

48. Wang R, Ghahary A, Shen Q, Scott PG, Roy K, et al. (2000) Hypertrophic scar tissues and fibroblasts produce more transforming growth factor-β1 mrna and protein than normal skin and cells. Wound Repair and Regeneration 8: 128–137.

49. Payne W, Wright T, Ko F, Wheeler C, Wang X, et al. (2003) Bacterial degradation of growth factors. J Appl Res 3: 35–40.

50. Brown KD, Friedkin M, Rozengurt E (1980) Colchicine inhibits epidermal growth factor degradation in 3t3 cells. Proceedings of the National Academy of Sciences 77: 480–484.

51. Yang L, Qiu CX, Ludlow A, Ferguson MW, Brunner G (1999) Active transforming growth factor-β in wound repair: determination using a new assay. The American Journal of Pathology 154: 105–111.

52. Lauffenburger DA, Horwitz AF (1996) Cell migration: a physically integrated molecular process. Cell 84: 359–369.

53. Ponugoti B, Xu F, Zhang C, Tian C, Pacios S, et al. (2013) Foxo1 promotes wound healing through the up-regulation of tgf-β1 and prevention of oxidative stress. The Journal of Cell Biology 203: 327–343.

54. Gibbs S, Silva Pinto AN, Murli S, Huber M, Hohl D, et al. (2000) Epidermal growth factor and keratinocyte growth factor differentially regulate epidermal migration, growth, and differentiation. Wound Repair and Regeneration 8: 192–203.

55. Pasonen-Seppänen S, Karvinen S, Törrönen K, Hyttinen JM, Jokela T, et al. (2003) Egf up-regulates, whereas tgf-β downregulates, the hyaluronan synthases has2 and has3 in organotypic keratinocyte cultures: correlations with epidermal proliferation and differentiation. Journal of Investigative Dermatology 120: 1038–1044.

56. Ibaraki N, Lin LR, Reddy VN (1995) Effects of growth factors on proliferation and differentiation in human lens epithelial cells in early subculture. Investigative Ophthalmology & Visual Science 36: 2304–2312.

57. Hebert TL, Wu X, Yu G, Goh BC, Halvorsen YDC, et al. (2009) Culture effects of epidermal growth factor (egf) and basic fibroblast growth factor (bfgf) on cryopreserved human adipose-derived stromal/stem cell proliferation and adipogenesis. Journal of Tissue Engineering and Regenerative Medicine 3: 553–561.

58. Ning M, Shui M, Khan B, Waqqar B, Benson B, et al. (1998) Effects of keratinocyte growth factor on the proliferation and radiation survival of human squamous cell carcinoma cell lines in vitro and in vivo. International Journal of Radiation Oncology Biology Physics 40: 177–187.

59. Nakazawa K, Yashiro M, Hirakawa K (2003) Keratinocyte growth factor produced by gastric fibroblasts specifically stimulates proliferation of cancer cells from scirrhous gastric carcinoma. Cancer Research 63: 8848–8852.